International Journal of Multiphase Flow 000 (2018) 1–15

Contents lists available at ScienceDirect

International Journal of Multiphase Flow

journal homepage: www.elsevier.com/locate/ijmulflow

Development of a three-dimensional phase-field lattice Boltzmann method for the study of immiscible fluids at high density ratios

T. Mitchell[a,*], C. Leonardi[a,b], A. Fakhari[c]

[a] School of Mechanical and Mining Engineering, The University of Queensland, St Lucia, QLD 4072, Australia
[b] Department of Civil and Environmental Engineering, Massachusetts Institute of Technology, 77 Massachusetts Avenue, Cambridge, MA 02139, USA
[c] Department of Chemical and Biomolecular Engineering, University of Pennsylvania, PA 19104, USA

ARTICLE INFO

Article history:
Received 1 December 2017
Revised 14 March 2018
Accepted 2 May 2018
Available online xxx

Keywords:
Lattice Boltzmann method
Multiphase flow
Phase-field modelling
Rayleigh–Taylor instability
Taylor bubble rise

ABSTRACT

Based on the recent work by Fakhari et al. (2017b), a three-dimensional phase-field lattice Boltzmann method was developed to investigate the rise of a Taylor bubble in a duct. The proposed approach couples the conservative phase-field equation with a velocity-based lattice Boltzmann scheme equipped with a weighted multiple-relaxation-time collision operator to enhance numerical stability. This makes the model ideal for numerical simulation of immiscible fluids at high density ratios and relatively high Reynolds numbers. Several benchmark problems, including the deformation of a droplet in a shear flow, the Rayleigh–Taylor instability, and the rise of a Taylor bubble through a quiescent fluid, were considered to asses the accuracy of the proposed solver. The Rayleigh–Taylor instability simulations were conducted for a configuration mimicking an air-water system, which has received little attention in the literature. After detailed verification and validation, the presented formulation was applied to study the flow field surrounding a Taylor bubble, for which numerical results were compared with the experimental work of Bugg and Saad (2002). The findings highlighted that the experimental bubble rise velocity, instantaneous flow field, and interface profile can be accurately captured by the presented model. In particular, the rise velocity of the present model indicated an improvement in accuracy when compared to the reference numerical solutions. The agreement between various numerical schemes, in some instances, indicated potential experimental difficulties in measuring the local flow field. Future application of the present model will facilitate detailed investigation of the pressure and flow profile surrounding Taylor bubbles evolving in co-current and counter-current flows.

1. Introduction

Multiphase fluid dynamics presents a number of challenges for both the development and application of practical computational techniques. The physically relevant properties range from the width of a two-fluid interface to the macroscopic flow behaviours of a system. Resolving all of the relevant length scales can increase computational overhead and render some multiphase solvers intractable. Additional difficulty arises when the two fluids in question have a large density contrast and are evolving at a high Reynolds number. This can generate steep numerical gradients across the fluid interface and deteriorate the stability of the applied mathematical model. Despite their complexity, high density ratio multiphase flows are commonplace in a number of industrial processes, and must be understood for efficient and safe operation of associated equipment. A particular example is observed in the oil and gas industry where the transport of multiphase fluids through pipes and or conduits is of great importance (Danielson, 2012). Two-phase slug flow is often observed in upstream operations, for which the modelling is typically examined through a series of slug units. Each unit consists of a Taylor bubble and a liquid slug, which propagate through the piping system. Lizarraga-Garcia et al. (2017) reported that discrepancies have been found between experimental data and closure relations for the rise velocity of the Taylor bubble in these slug units. This can strongly affect the prediction of pressure gradients and liquid holdup in a number of mechanistic models (Lizarraga-Garcia et al., 2017; Wu et al., 2017). To this end, the primary objective of this work is to analyse the flow physics of a propagating Taylor bubble. This is performed using a newly developed, three-dimensional phase-field lattice Boltzmann method for immiscible fluids at high density ratios.

* Corresponding author.
E-mail address: t.mitchell@uq.edu.au (T. Mitchell).

https://doi.org/10.1016/j.ijmultiphaseflow.2018.05.004
0301-9322/

The development of numerical models capable of accurately assessing the dynamics of high density ratio flows is an area of ongoing research. To help ameliorate the numerical singularity of fluid properties at the moving interface, while still modelling practical scales, this study takes a diffuse-interface approach based on phase-field theory. In this, the sharp interface is replaced by a smoothly transitioning region over which the fluid parameters change rapidly, but continuously. This removes the singularity of a bounding interfacial surface and replaces it with volumetric forces, which tend to zero in the bulk fluid regions. Phase-field methods approach the problem of interface tracking through a minimisation of free energy which differs from other commonly seen interface-tracking methods such as the level-set (Osher and Sethian, 1988) or the volume-of-fluid method (Hirt and Nichols, 1981), which look to directly minimise the interfacial surface area through its geometric properties. This study employs the conservative phase-field approach proposed by Chiu and Lin (2011). This model has been reformulated in the lattice-Boltzmann equation (LBE) (Geier et al., 2015a) and further developed and analyzed in the literature (Fakhari et al., 2016b). The recent work by Fakhari et al. (2017b) utilised this phase-field approach and coupled it with a velocity-based lattice Boltzmann scheme similar to that proposed by Zu and He (2013). Results showed that the formulation was capable of accurately capturing both high density ratio and high Reynolds number situations within two-dimensional (2D) flow configurations. Additionally, the improved locality of the method in relation to certain other phase field formulations increased computational efficiency on GPU architectures. Therefore, a secondary objective of this study was to extend this model into three-dimensions (3D) and show that the robustness observed in 2D could be maintained.

Over the past few decades, the LBM for multiphase flows has been developed and applied to simulate bubble dynamics (Amaya-Bower and Lee, 2010), contact line dynamics (Lee and Liu, 2010), drop impact dynamics (Lycett-Brown et al., 2014), and porous media flows (Liu et al., 2016). The most popular models present in the literature can be grouped into four major classes, namely the colour-gradient (Gunstensen et al., 1991), pseudo-potential (Shan and Chen, 1993; Shan and Doolen, 1995), free-energy (Swift et al., 1995; 1996), and mean-field or phase-field methods (He et al., 1999; Jacqmin, 1999). Although a large amount of work has been conducted using these models, there exists limited literature documenting their validation against experimental results, particularly at high-density ratios. This issue is partly rectified in this study through a detailed comparison of Taylor bubble flow with the experimental work of Bugg and Saad (2002) and the numerical work of Ndinisa et al. (2005).

The colour-gradient model originated from work previously conducted in the lattice-gas model, and was introduced into the LBM to simulate immiscible binary fluids. Grunau et al. (1993) modified the original work, extending it to handle both density and viscosity variations. These early studies using the colour-gradient model were performed on a hexagonal lattice in 2D. Ries and Phillips (2007) developed the D2Q7 model of Grunau et al. (1993) on a D2Q9 lattice and incorporated a two-phase collision operator. This modified perturbation operator enabled them to recover the correct interfacial force term, which ensured compatibility between the interfacial tension and the capillary stress tensor. An extension of this work led to a generalised perturbation operator introduced by Liu et al. (2012) for the D3Q19 lattice. For the colour-gradient model to maintain an interface, as well as to encourage phase segregation, a recolouring step is required in the algorithm. There are two predominant methods used for this, but that of Latva-Kokko and Rothman (2005) was recently shown by Leclaire et al. (2012) to have improved numerical stability and accuracy across a range of benchmark simulations. Anwar (2013) was able to show the ability of the colour-gradient model to capture the behaviour of rising bubbles under a range of fluid properties in comparison with simulations run using the level set method available in COMSOL Multiphysics. Here, the density contrast was limited to $O(10)$, but an effective buoyancy force was used to capture a wide variety of dimensionless parameters. Significant work has been undertaken to enhance the colour-gradient model, but recently proposed models such as that by Leclaire et al. (2017) still report difficulty in achieving high density ratios in complex scenarios. It has been reported that the state-of-the-art colour-gradient models in this category, although very good for liquid-liquid interfaces, are limited to relatively simple liquid-gas flows at low Reynolds numbers (Leclaire et al., 2017).

With a relatively simplistic underlying algorithm, the pseudo-potential model initially proposed by Shan and Chen (1993) has remained arguably the most popular multiphase LBM. The model exists in two forms, namely single-component multiphase (SCMP) (Shan and Chen, 1994) and multi-component multiphase (MCMP) (Shan and Chen, 1993; Shan and Doolen, 1995). The model relies on the incorporation of particle interactions within the LB framework to induce phase separation. These original models suffered from well reported limitations such as low density ratios, spurious currents, and non-physical interdependency of parameters (Liu et al., 2016). With recent advances (Yuan and Schaefer, 2006; Kupershtokh et al., 2009; Porter et al., 2012; Montessori et al., 2015; Lycett-Brown and Luo, 2016; Ammar et al., 2017), the complexity of the model has increased, but so too has its applicability to fluid flows with high density and viscosity ratios. Yuan and Schaefer (2006) were amongst the first to incorporate various equations of state within the pseudopotential framework. Montessori et al. (2015) reported that with the use of a Carnahan–Starling equation of state and a D3Q27-F93 lattice (F93 refers to 93 discrete velocities used in force calculation), the pseudo-potential model could simulate liquid-vapour interfaces with density ratio over 1000 with low spurious currents. Lycett-Brown and Luo (2016) later reported results on binary droplet collisions with a density ratio of 1000, without the need for additional discrete velocities. In their work, the so called multiple-relaxation time cascaded collision operator was used and found to significantly enhance the stability of the pseudo-potential method proposed (Leclaire et al., 2017). The improvements developed by such authors have greatly increased the range of applicable cases for the pseudopotential model, which is evident in its popularity in the literature. However, to date there still remains a limited number of high density ratio, dynamic benchmark cases for this model.

In the context of the lattice Boltzmann method, the free-energy model and, as a subclass, the phase-field model have recently attracted attention in the literature for the simulation of multiphase flow problems. Although the difference in these models is somewhat cosmetic, they are often referenced independently in the lattice Boltzmann literature. This is a consequence of how the early models were formulated. Arguably the most obvious difference between these is the interface-tracking parameter. In the early free-energy models, the fluid density was used for this purpose which is in contrast to the phase-field model where an index function is used. Furthermore, the governing equation to capture the interface dynamics in the free-energy model is the continuity equation with additional low order terms. The evolution of the phase-field index function is typically governed by the Cahn–Hilliard (or the Allen–Cahn) equation. The phase-field model provides a systematic relationship between the surface tension, interfacial thickness, and chemical potential which is not clear in the primitive forms of the free energy models. Although the phase-field model can be considered as a subclass of the free-energy model, a deliberate distinction has been made to highlight the per-

Please cite this article as: T. Mitchell et al., Development of a three-dimensional phase-field lattice Boltzmann method for the study of immiscible fluids at high density ratios, International Journal of Multiphase Flow (2018), https://doi.org/10.1016/j.ijmultiphaseflow.2018.05.004

spectives from which they were derived. The phase-field model, as described in this work, was developed from Jacqmin (1999, 2000) whilst the free-energy LBM had been previously introduced by Swift et al. (1995, 1996). Since their first appearance in the literature, there have been a number of model variations proposed. Here the free-energy models by Inamuro et al. (2004) and (ZSC) Zheng et al. (2006), as well as the phase-field models of Lee and Lin (2005), and Zu and He (2013) are deliberately highlighted. Inamuro *et al.* proposed a model capable of simulating relatively high density ratio flows, but required pressure to be found through solving a Poisson equation. This proved to be computationally demanding with the time to convergence increasing with density ratio. Later, the ZSC model was proposed with a particle distribution function for the mean density and momentum to overcome issues surrounding Galilean invariance for the free-energy model. However, Fakhari and Rahimian (2010) showed that the model is only valid for density-matched binary fluids. The model by Lee and Lin (2005) was able to overcome some of the numerical difficulties of density contrast by taking an incompressible transformation to change the particle distribution function into one for pressure and momentum. This was originally proposed in the mean-field model by He et al. (1999), but Lee and Lin (2005) were able to enhance numerical stability through certain discretisation schemes. The phase-field model has seen significant enhancement since its introduction (Lee et al., 2006; Lee and Liu, 2010; Fakhari and Lee, 2013; Fakhari et al., 2016b), now overcoming much of the initial criticisms such as the violation of conservation properties.

As previously stated, the specific model used in this study implements a velocity-based LBM to recover the hydrodynamics, modified from Zu and He (2013) by Fakhari et al. (2017b), which is extended herein to 3D. This method maintains a high level of locality with the phase field representing the only non-local quantity required in the collision step. To maintain stability of the method at large viscosity contrasts and or high Reynolds numbers, the weighted multiple-relaxation-time (WMRT) collision model (Fakhari et al., 2017a) is incorporated into the formulation. This work does not focus on the use of different collision operators and their impact on stability. However, developments such as the cumulant (Geier et al., 2015b) and entropic LBM (Ansumali et al., 2003; Mazloomi et al., 2015; Atif et al., 2017) have also emerged in recent years as promising tools for stabilising hydrodynamic simulations. The interface evolution is captured with the use of a second distribution function to solve the conservative phase-field equation as done by Geier et al. (2015a). The model has been implemented in the open-source software TCLB (Łaniewski-Wołłk and Rokicki, 2016), which has been used to perform the simulations presented in this study.

The remainder of this paper is organised as follows. In Section 2 the governing equations for hydrodynamics and interface evolution for immiscible two-phase flows are introduced. The lattice Boltzmann algorithm used to solve these equations is given in Section 3, along with the numerical details required for implementation. The results obtained using the presented numerical scheme are given in Section 4, wherein the model is first verified against the work of Leclaire et al. (2017) for droplet deformation in a density-matched binary fluid. The 3D Rayleigh–Taylor instability is the second test case investigated, in which the current results are compared with the work of Zu and He (2013) and He et al. (1999) at low Reynolds number and small density contrast. The true advantage of the model is then shown by simulating the Rayleigh–Taylor instability at a relatively high Reynolds number with fluid properties similar to that of an air-water system. This particular case extends beyond previous literature, providing reference data for future testing of advanced models. Finally, the model is validated via comparison with the experimental work of Bugg and Saad (2002), analysing the rise of a Taylor bubble. This experimental case has previously been used to validate finite-volume methods in commercial codes such as ANSYS CFX 5.6 by Ndinisa et al. (2005) and ASCOMP's TransAT by Lizarraga-Garcia et al. (2017). The model is observed to accurately capture the experimental findings, indicating its potential applicability to modelling multiphase transport through tubular geometries. Section 5 draws final conclusions from this work and outlines the direction of future research.

2. Governing equations

In this study the conservative phase field model (Geier et al., 2015a) is coupled with the Navier–Stokes and continuity equations to investigate multiphase flow problems. The phase field model originates from the work of Chiu and Lin (2011) whom formulated the modified Allen-Cahn equation (ACE) proposed by Sun and Beckermann (2007) in a conservative form. Later, Geier et al. (2015a) presented the phase field version of this within the lattice Boltzmann framework. The phase field variable, ϕ, assumes two extreme values in the light phase, ϕ_L, and in the heavy phase, ϕ_H. The interface location is taken as the average value of ϕ, given by $\phi_0 = (\phi_H + \phi_L)/2$. The equation that governs the evolution of the interface in this model is given by Chiu and Lin (2011),

$$\partial_t \phi + \nabla \cdot \phi \boldsymbol{u} = \nabla \cdot M\left(\nabla\phi - \frac{1-4(\phi-\phi_0)^2}{W}\boldsymbol{n}\right), \tag{1}$$

where $\boldsymbol{u}$ is the macroscopic velocity vector, M is the mobility, W describes the interfacial width, and $\boldsymbol{n} = \nabla\phi/|\nabla\phi|$ is the unit vector normal to the interface. The profile of the phase field over the diffuse interface is assumed to vary by,

$$\phi(\boldsymbol{x}) = \phi_0 \pm \frac{\phi_H - \phi_L}{2}\tanh\left(\frac{2|\boldsymbol{x}-\boldsymbol{x_0}|}{W}\right), \tag{2}$$

where $\boldsymbol{x_0}$ indicates the interface location.

For the two-phase flow systems in this work, the phase-field variable ϕ is defined to take a value of one in the heavy fluid, $\phi_H = 1$, and a value of zero in the lighter fluid, $\phi_L = 0$. The bounds of ϕ are chosen to reduce the effect of compressibility in the low density phase (Fakhari et al., 2017b). In order to determine the local density from the phase field, a simple linear interpolation between the light fluid, ρ_L, and the heavy fluid, ρ_H, is made,

$$\rho = \rho_L + \phi(\rho_H - \rho_L). \tag{3}$$

The hydrodynamics of an incompressible multiphase flow is defined by the well-known continuity and momentum equations,

$$\nabla \cdot \boldsymbol{u} = 0, \tag{4}$$

$$\rho\left(\partial_t \boldsymbol{u} + \boldsymbol{u}\cdot\nabla\boldsymbol{u}\right) = -\nabla p + \nabla\cdot\Pi + \mathbf{F}, \tag{5}$$

where ρ is the fluid density, p is the hydrodynamic pressure, $\Pi = \mu\left[\nabla\boldsymbol{u} + (\nabla\boldsymbol{u})^T\right]$ is the viscous stress tensor, μ is the dynamic viscosity, and $\mathbf{F} = \mathbf{F}_s + \mathbf{F}_b$ is the volumetric force. The terms $\mathbf{F}_s$ and $\mathbf{F}_b$ represent the forces associated with the surface tension and body forces in the system, respectively. Various formulations for these forces exist, but in this work they are defined as (Jacqmin (2000)),

$$\mathbf{F}_s = \mu_\phi \nabla\phi, \tag{6}$$

with

$$\mu_\phi = 1.5\sigma\left[32\phi(\phi-1)(\phi-0.5)/W - W\nabla^2\phi\right], \tag{7}$$

where μ_ϕ is the chemical potential and σ is the surface tension, and

$$\mathbf{F}_b = \rho\boldsymbol{g}, \tag{8}$$

where $\boldsymbol{g}$ is the gravitational acceleration.

Please cite this article as: T. Mitchell et al., Development of a three-dimensional phase-field lattice Boltzmann method for the study of immiscible fluids at high density ratios, International Journal of Multiphase Flow (2018), https://doi.org/10.1016/j.ijmultiphaseflow.2018.05.004

3. Lattice Boltzmann formulation

In order to recover the conservative phase-field equation in 3D, the D3Q15 lattice structure is used for which a lattice population, h_i, is defined. The single-relaxation-time collision operation is performed for the phase-field population. The hydrodynamics on the other hand is recovered using the D3Q27 lattice with the population g_i. For this, the WMRT scheme is applied (Fakhari et al., 2017a) allowing the model to achieve relatively large viscosity contrasts and high Reynolds numbers. Here it can be seen that a lower order stencil is applied for the conservative phase field model to reduce computational costs. The applicability of the D3Q15 lattice structure to evaluate the model was shown in Fakhari et al. (2016a). This stencil allows the resolution of the zeroth- and first-order moments, which is sufficient for modelling the phase-field equation. However, for the hydrodynamics, the D3Q27 lattice improves the isotropy and can assist in solution accuracy and stability. For these standard lattice structures on a uniform grid, it is common practice to take the underlying lattice length, δx, and time, δt, scales such that $\delta x = \delta t = 1$ lattice unit (lu) and $c = \delta x/\delta t = 1$. The mesoscopic lattice velocities, $\boldsymbol{c}_i$, and weights, w_i, are given in Appendix A, and the WMRT transformation matrix is supplied in Appendix B.

3.1. Conservative phase-field LBE

The LBE for tracking the fluid-fluid interface is given by Fakhari et al. (2017a) as

$$h_i(\boldsymbol{x}+\boldsymbol{c}_i\delta t, t+\delta t) = h_i(\boldsymbol{x},t) - \frac{h_i(\boldsymbol{x},t)-\bar{h}_i^{\mathrm{eq}}(\boldsymbol{x},t)}{\tau_\phi+1/2} + F_i^{\phi}(\boldsymbol{x},t), \quad (9)$$

where $\tau_\phi = M/c_s^2$ is the phase-field relaxation time with the speed of sound of the system, $c_s = c/\sqrt{3}$. The forcing term is defined as

$$F_i^{\phi}(\boldsymbol{x},t) = \delta t \frac{4\phi(1-\phi)}{W} w_i \boldsymbol{c}_i \cdot \boldsymbol{n}, \quad (10)$$

when one takes the extreme values of ϕ as $\phi_{\mathrm{H}} = 1$ and $\phi_{\mathrm{L}} = 0$.

The term $\bar{h}_i^{\mathrm{eq}}$ signifies that the equilibrium distribution is shifted by the forcing term

$$\bar{h}_i^{\mathrm{eq}}(\boldsymbol{x},t) = h_i^{\mathrm{eq}} - \frac{1}{2}F_i^{\phi}, \quad (11)$$

where

$$h_i^{\mathrm{eq}} = \phi w_i \left(1 + \frac{\boldsymbol{c}_i\cdot\boldsymbol{u}}{c_s^2} + \frac{(\boldsymbol{c}_i\cdot\boldsymbol{u})^2}{2c_s^4} - \frac{\boldsymbol{u}\cdot\boldsymbol{u}}{2c_s^2}\right). \quad (12)$$

To relate the interface-tracking distribution function h_i to the phase-field variable, its zeroth moment is taken after the streaming step,

$$\phi = \sum_i h_i. \quad (13)$$

3.2. Velocity-based LBM

The LBE used in this study was proposed by Fakhari et al. (2017b) to improve the velocity-based LBM developed by Zu and He (2013). The improvements aimed to increase the efficiency of the Zu and He approach (Zu and He, 2013) by eliminating the need to directly calculate velocity gradients using finite difference stencils, instead extracting the deviatoric stress tensor from the higher-order moments of the LBM itself. Additionally, the need for a predictor-corrector step to determine pressure and velocity was removed by simplifying the equilibrium distribution function. The robustness of the current LBM was exhibited in 2D with numerous test cases at both high-density contrasts and relatively high Reynolds numbers (Fakhari et al., 2017b). Here the 3D algorithm is described with the addition of a WMRT collision operator.

The LBE to recover Eq. (5) is given by

$$g_i(\boldsymbol{x}+\boldsymbol{c}_i\delta t, t+\delta t) = g_i(\boldsymbol{x},t) - \mathbf{M}^{-1}\hat{\mathbf{S}}\mathbf{M}\left[g_i(\boldsymbol{x},t) - \bar{g}_i^{\mathrm{eq}}(\boldsymbol{x},t)\right] + F_i(\mathbf{x},t), \quad (14)$$

in which the equilibrium distribution, g_i^{eq} is shifted in the same sense as the phase-field distribution, for the inclusion of the forcing term

$$\bar{g}_i^{\mathrm{eq}}(\boldsymbol{x},t) = g_i^{\mathrm{eq}} - \frac{1}{2}F_i, \quad (15)$$

with

$$g_i^{\mathrm{eq}} = w_i\left[p^* + \left(\frac{\boldsymbol{c}_i\cdot\boldsymbol{u}}{c_s^2} + \frac{(\boldsymbol{c}_i\cdot\boldsymbol{u})^2}{2c_s^4} - \frac{\boldsymbol{u}\cdot\boldsymbol{u}}{2c_s^2}\right)\right], \quad (16)$$

where $p^* = p/\rho c_s^2$ is the normalised pressure. The orthogonal transformation matrix, $\mathbf{M}$, is given in Appendix B and the diagonal relaxation matrix is

$$\hat{\mathbf{S}} = \mathrm{diag}(1,1,1,1,s_\nu,s_\nu,s_\nu,s_\nu,1,\ldots,1) \quad (17)$$

for the defined transformation matrix. The relaxation parameter $s_\nu = (\tau+0.5)^{-1}$ relates the hydrodynamic relaxation time, τ, to the viscosity according to

$$\mu = \rho\nu = \rho\tau c_s^2, \quad (18)$$

where ν is the kinematic viscosity. The relaxation time can be calculated via interpolation, with a number of forms proposed and examined in the literature (Fakhari et al., 2017b). In this study, a linear interpolation is used such that

$$\tau = \tau_{\mathrm{L}} + \phi(\tau_{\mathrm{H}} - \tau_{\mathrm{L}}), \quad (19)$$

where τ_{L} and τ_{H} are the bulk relaxation times in the light and heavy fluids, respectively. The values for these relaxation times are determined using the viscosities of each fluid via Eq. (18).

The hydrodynamic forcing term is given by

$$F_i(\boldsymbol{x},t) = w_i\frac{\boldsymbol{c}_i\cdot\mathbf{F}}{\rho c_s^2}, \quad (20)$$

where the forcing term $\mathbf{F}$ accounts for surface tension and body forces given in Eq. (6) and Eq. (8), respectively. In addition, a pressure, $\mathbf{F}_{\mathrm{p}}$, and viscous, $\mathbf{F}_\mu$, force is required to recover Eq. (5) as a result of the velocity-based formulation (Zu and He, 2013),

$$\mathbf{F} = \mathbf{F}_{\mathrm{s}} + \mathbf{F}_{\mathrm{b}} + \mathbf{F}_{\mathrm{p}} + \mathbf{F}_\mu. \quad (21)$$

From a Chapman–Enskog type analysis, the pressure force can be determined to be (Fakhari et al. (2017b)),

$$\mathbf{F}_{\mathrm{p}} = -p^* c_s^2(\rho_{\mathrm{H}} - \rho_{\mathrm{L}})\nabla\phi, \quad (22)$$

and the viscous force as (Fakhari et al. (2017b))

$$\mathbf{F}_\mu = \nu(\rho_{\mathrm{H}} - \rho_{\mathrm{L}})\left[\nabla\boldsymbol{u} + (\nabla\boldsymbol{u})^T\right]\cdot\nabla\phi, \quad (23)$$

wherein the derivatives of velocity are recovered from the second moment of the hydrodynamic distribution function,

$$F_{\mu,\alpha} = -\frac{\nu(\rho_{\mathrm{H}} - \rho_{\mathrm{L}})}{c_s^2}\left[\sum_i c_{i,\alpha}c_{i,\beta}\sum_j(\mathbf{M}^{-1}\hat{\mathbf{S}}\mathbf{M})_{i,j}(g_i - g_i^{\mathrm{eq}})\right]\partial_\beta\phi. \quad (24)$$

The gradient and Laplacian of the phase-field variable are determined using all the neighbouring nodes and are defined as (Kumar, 2004; Ramadugu et al., 2013; Thampi et al., 2013),

$$\nabla\phi = \frac{c}{c_s^2\delta x}\sum_{i=0}^{26}\boldsymbol{c}_i w_i \phi(\boldsymbol{x}+\boldsymbol{c}_i\delta t, t), \quad (25)$$

Please cite this article as: T. Mitchell et al., Development of a three-dimensional phase-field lattice Boltzmann method for the study of immiscible fluids at high density ratios, International Journal of Multiphase Flow (2018), https://doi.org/10.1016/j.ijmultiphaseflow.2018.05.004

$$\nabla^2\phi = \frac{2c^2}{c_s^2(\delta x)^2}\sum_{i=0}^{26} w_i[\phi(\boldsymbol{x}+\boldsymbol{c}_i\delta t, t) - \phi(\boldsymbol{x}, t)], \tag{26}$$

respectively.

The macroscopic properties recovered from the hydrodynamic distribution function are

$$p^* = \sum_i g_i, \tag{27}$$

$$\boldsymbol{u} = \sum_i g_i\boldsymbol{c}_i + \frac{\mathbf{F}}{2\rho}. \tag{28}$$

4. Results

4.1. Droplet deformation in shear flow

To start benchmarking the 3D phase-field LBM presented in this work, the deformation of a droplet placed in a shear flow is first analysed. This test case can be found in numerous works in the literature (Taylor, 1934; Shapira and Haber, 1990; Xi and Duncan, 1999; Inamuro et al., 2002), but here particular note is taken of the work by Leclaire et al. (2017). Here the authors sought to compare the colour-gradient and pseudopotential LB models across numerous test cases. Using a droplet in shear flow they were able to show that both models were capable of reproducing analytical relations in the small capillary number limit. They noted that the colour-gradient model showed good stability and accuracy for a larger range of parameters than those obtained with the chosen pseudopotential model. The aim of this section is to include a phase-field model into this benchmark case through applying a similar test methodology. As such, a domain, $\mathcal{D}$ is defined consistently with the work of Leclaire et al. (2017) such that

$$\mathcal{D} = (x, y, z) \in [0, X] \times [0, Y] \times [0, Z]. \tag{29}$$

A spherical interface with radius R is initialised with centroid ($X/2$, $Y/2$, $Z/2$). To do this, the phase-field is specified by

$$\phi_{x,y,z} = \frac{1}{2}\left[1 - \tanh\left(\frac{|\boldsymbol{x}-\boldsymbol{x_0}| - R}{W/2}\right)\right], \tag{30}$$

where $\boldsymbol{x}$ is the spatial location and $\boldsymbol{x_0}$ is the center of the spherical droplet. For simplicity, the number of dimensionless parameters associated with this problem is reduced by defining the following geometric ratios (Leclaire et al., 2017): $X/Z = 2$, $Y/Z = 1$ and $R/Z = 0.2$. Additionally, the density and viscosity ratios are both set to unity while the interface width W is set to three lattice units. With these values, the bubble deformation D becomes a function of the capillary and Reynolds numbers only, defined respectively as

$$\mathrm{Ca} = \frac{\dot{\gamma}R\mu_\mathrm{H}}{\sigma}, \tag{31}$$

$$\mathrm{Re} = \frac{\dot{\gamma}R^2\rho_\mathrm{H}}{\mu_\mathrm{H}}, \tag{32}$$

where $\dot{\gamma} = 2U/Z$ is the shear rate due to an imposed velocity U at the top and $-U$ at the bottom of the domain. To provide results over a range of Ca, the same approach used by Leclaire et al. (2017) is taken, in which μ_H is held constant and the surface tension σ is varied. To characterise the final degree of freedom associated with the diffuse interface model, an interface Peclet number is defined as (Komrakova et al. (2014)),

$$\mathrm{Pe}_{int} = \frac{\dot{\gamma}RW}{M}. \tag{33}$$

This is used to relate the convective and diffusive time scales of the interface. For this study of droplet deformation, the mobility is specified as $M = 0.2$ for all Re and Ca tested. For a detailed analysis on the effect of Pe_{int}, the interested reader is pointed towards the work of van der Sman and van der Graaf (2008) as well as the more recent study by Komrakova et al. (2014).

With the geometric constraints stated, the original analysis describing the bubble deformation conducted by Taylor (1934) breaks down with the $R/Z \ll 1$ assumption being invalid. Since his seminal study, numerous authors have utilised perturbation theory to gain further understanding of the system. The work of Shapira and Haber (1990), for example, incorporated a corrective term in Taylor's formulation to account for wall effects. The expression for bubble deformation from their analysis was expressed for Stokesian flows ($\mathrm{Re} \ll 1$) and was found to be

$$D = \frac{19\kappa + 16}{16\kappa + 16}\mathrm{Ca}\left[1 + C_{sh}\frac{2.5\kappa + 1}{\kappa + 1}\left(\frac{R}{Z}\right)^3\right], \tag{34}$$

where $\kappa = \mu_\mathrm{H}/\mu_\mathrm{L}$ and $C_{sh} = 5.6996$ is the corrective wall term for a droplet centered in the domain. Here, it is highlighted that the wall effects incorporated in the analytical works of Shapira and Haber (1990) are derived to $O(\mathrm{Ca})$. As such, it is expected that the results will deteriorate progressively with increasing capillary number. In this work, results are reported for Reynolds numbers between 0.05 and 0.2 for capillary numbers ranging between 0.02 and 0.3. If one takes $C_{sh} = 0$, the original form proposed by Taylor (1934) is recovered,

$$D = \mathrm{Ca}\frac{19\kappa + 16}{16\kappa + 16}. \tag{35}$$

Taking note from Leclaire et al. (2017), the grid resolution is specified based on an input parameter, r, and a constant, $N_0 = 50$, such that

$$N_x = 2rN_0 - 2, \tag{36}$$

$$N_y = rN_0, \tag{37}$$

$$N_z = rN_0 - 1. \tag{38}$$

Here, $N_{x,\,y,\,z}$ are the number of nodes in X, Y, and Z, respectively. A node is subtracted from the periodic axis to enforce the geometric requirements of X/Z and Y/Z for the domain extents. For simplicity, velocity boundary conditions on the top and bottom of the domain are implemented by assuming bounce-back of the non-equilibrium parts of the hydrodynamic population g_i (Hecht and Harting, 2010).

An alternative approach was taken to analyse the deformation results in comparison with the work of Leclaire et al. (2017), whom formulated the analysis as an optimisation problem. To do this, a contour indicating the center of the interface was found and an optimisation problem was solved for the shortest and longest distances to the centre of the ellipse (*i.e.* major and minor axes). The authors then used two additional contours in the interface and performed a similar analysis to determine the angle of rotation. In this work, an ellipsoidal shape is fit to the contour given at $\phi = 0.5$, and then the parameters of the function are utilised to determine the major and minor axes.

Fig. 1(a) compares the results of the present phase-field LBM using $r = 1$ with the analytical results of Shapira and Haber (1990) and the numerical results of Leclaire et al. (2017). Here it is clear that the phase-field model is in agreement with the results obtained using the colour gradient model. The results also reinforce the findings of the previous works, where accurate matching of analytical results is seen in the limit of small Ca number. However, at higher Ca, it is evident that the predicted deformation departs significantly from the analytical solution for small

Please cite this article as: T. Mitchell et al., Development of a three-dimensional phase-field lattice Boltzmann method for the study of immiscible fluids at high density ratios, International Journal of Multiphase Flow (2018), https://doi.org/10.1016/j.ijmultiphaseflow.2018.05.004

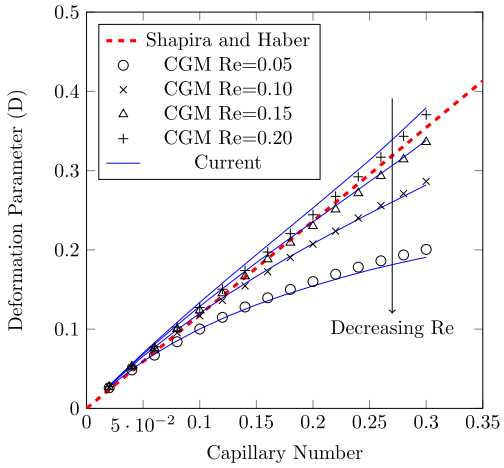

(a) Resolution, $r = 1$

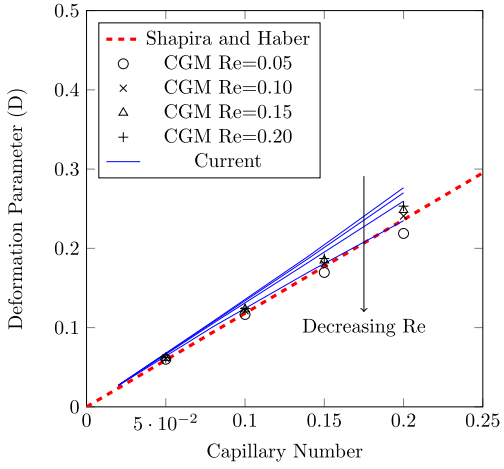

(b) Resolution, $r = 2$

Fig. 1. Comparison of the colour-gradient model results presented in Leclaire et al. (2017) (markers) with those from the 3D phase-field LBM proposed in this work (solid lines) with all simulations conducted at a resolution of (a) $r = 1$ and (b) $r = 2$. The arrows indicate the Re for the 'Current' solutions decreasing from 0.2 to 0.05.

Re. This appears contradictory to the Shapira and Haber correction that is specifically valid for $\mathrm{Re} \ll 1$. In this case, it appears evident that the resolution $r = 1$, is insufficient to capture the flow characteristics for Ca greater than approximately 0.075. This is clear from the increased resolution results in Fig. 1(b), in which results progressively improve for decreasing Re for all Ca tested.

A particular point highlighted by Leclaire et al. (2017) was the fact that, in contrast to the pseudo-potential LBM, the colour-gradient model was able to achieve a constant interface width across the range of Ca and Re numbers. This is also achieved using the phase-field LBM with direct control given by the interface width parameter W. What was not investigated however, was the effect of the interface width on the deformation of the droplet. To study this relation, a series of tests were conducted at $\mathrm{Ca} = 0.02$. The interface width was varied from three to nine and Re between 0.05 and 0.20, while the remaining parameters were kept consistent with the previous test. Fig. 2 displays the deterioration of results with increasing interface thickness, particularly for the resolution of $r = 1$. This behaviour is expected as the simulations tend away from the sharp interface limit. For the results at resolution $r = 2$, a similar trend is observed until $W = 3$. At which point, a minor deterioration of accuracy is observed for all Re.

4.2. Rayleigh–Taylor instability

To demonstrate the accuracy and stability of the model in 3D, the Rayleigh–Taylor instability represents a common benchmark. This phenomenon occurs when a heavy fluid is situated above a lighter fluid within a gravitational field, and the interface between the two is subject to a perturbation. In this configuration, the heavy fluid is observed to penetrate into the lighter fluid, for which the characteristics of motion have been investigated by many authors (He et al., 1999; Zu and He, 2013; Li et al., 2012; Shao and Shu, 2015; Ren et al., 2016; Fakhari et al., 2017b).

The previous work of Fakhari et al. (2017b) demonstrated that the presented model could accurately simulate the Rayleigh–Taylor instability up to high density ratios ($\rho^* = 1000$) and relatively high Reynolds numbers ($\mathrm{Re} = 3000$) in two-dimensions. As such, the instability provides a reasonable test case for which to analyse the three-dimensional extension of the model.

The construction of the flow domain for this case consists of a rectangular prism given by,

$$\mathcal{D} = (x, y, z) \in [-L/2, L/2] \times [-2L, 2L] \times [-L/2, L/2]. \tag{39}$$

For the base case, the model parameters were chosen according to the work of Zu and He (2013), with $L = 128$ and dimensionless parameters including Atwood number, At, Reynolds number, Re, and capillary number, Ca, defined as

$$\mathrm{At} = \frac{\rho_\mathrm{H} - \rho_\mathrm{L}}{\rho_\mathrm{H} + \rho_\mathrm{L}} = 0.5, \tag{40}$$

$$\mathrm{Re} = \frac{L\sqrt{gL}}{\nu} = 128, \tag{41}$$

$$\mathrm{Ca} = \frac{\mu_\mathrm{H}\sqrt{gL}}{\sigma} = 9.1. \tag{42}$$

From the definitions above, it is clear that At describes the density ratio, Re indicates the relative effect of gravitational to viscous forces, and Ca is the relative effect of viscous forces to surface tension. To close the dimensionless system, the kinematic viscosities of the two fluids are specified to be equal ($\nu^* = 1$), giving a viscosity ratio of three ($\mu^* = 3$). Additionally, the numerical Péclet number is

$$\mathrm{Pe} = \frac{L\sqrt{gL}}{M} = 744, \tag{43}$$

and a reference time is defined as $t_0 = \sqrt{L/g} = 6000$ such that $t^* = t/t_0$ is the dimensionless time. In order to initiate the Rayleigh–Taylor instability, the interface between the two-fluids is initially perturbed by

$$y(x, z) = 0.05L \times (\cos(2\pi x/L) + \cos(2\pi z/L)). \tag{44}$$

After initialisation, a constant acceleration applied to the system causes the heavy fluid to penetrate into the lighter fluid. Fig. 3 shows the evolution of the interface at dimensionless times $t^* = 1$, 2, 3, 4 and 4.5, with the colour contour (online) based on the local velocity magnitude. The definitions of the points tracked in the simulation are also found on this figure, namely the bubble, spike, and saddle points of the initial perturbation. Qualitatively, similar results to those obtained by Zu and He (2013) are observed. The saddle points are the first to display the roll-up like behaviour with the mushroom-like shape forming at the spike shortly after.

A quantitative comparison is performed by tracking the position of the bubble, spike, and saddle points through the simulation in order to compare with the works of Zu and He (2013) and

Please cite this article as: T. Mitchell et al., Development of a three-dimensional phase-field lattice Boltzmann method for the study of immiscible fluids at high density ratios, International Journal of Multiphase Flow (2018), https://doi.org/10.1016/j.ijmultiphaseflow.2018.05.004

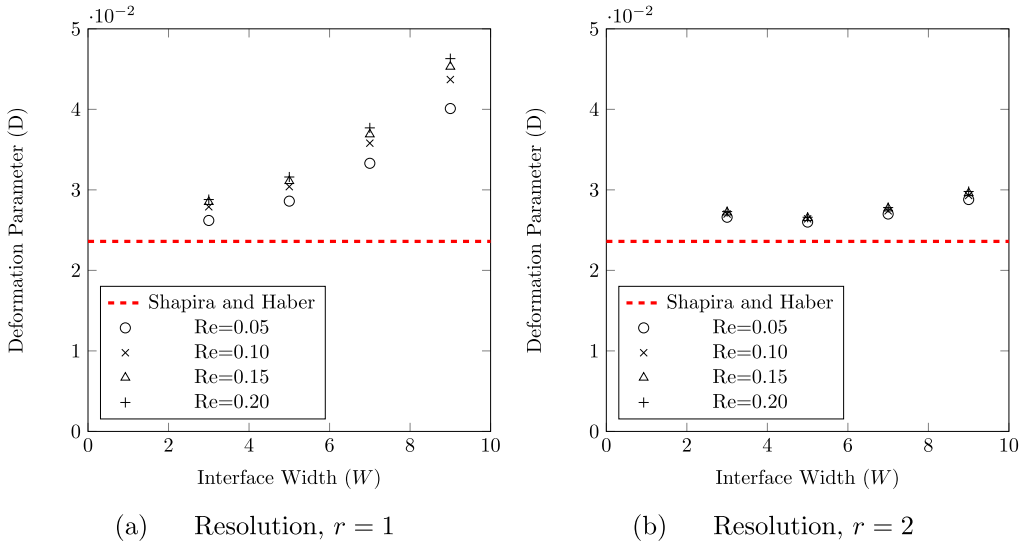

Fig. 2. Variation of the deformation parameter with interface width for Ca = 0.02 at (a) $r = 1$ and (b) $r = 2$.

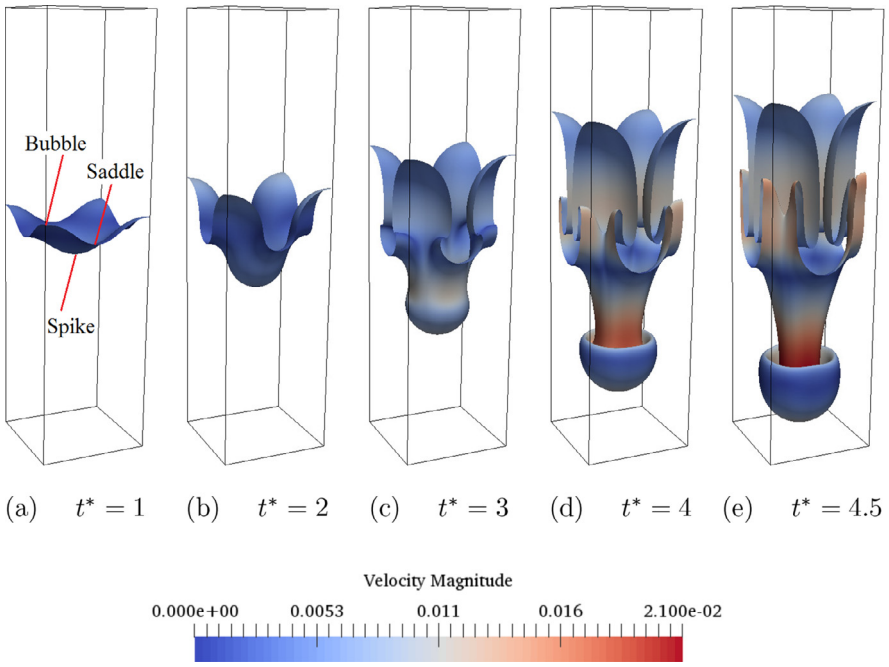

Fig. 3. The evolution of the three-dimensional Rayleigh–Taylor instability with flow conditions defined by At = 0.5, Re = 128, $\mu^* = 3$, Ca = 9.1, and Pe = 744.

He et al. (1999). Fig. 4(a) shows a close agreement with these studies, showing the accuracy of the 3D model. However, this flow scenario features both a low Reynolds number and low density ratio, with neither of the previous studies extending their analysis beyond this for the 3D case. Therefore, another case with the viscosity and density ratios similar to that found in an air-water system ($\rho^* = 1000$, $\mu^* = 100$) is considered with a Reynolds number of 3000. As per the previous case, the characteristic length scale is taken as $L = 128$. However, the reference time is reduced to $t_0 = 4000$ to maintain a similar capillary number at Ca = 8.7. A density ratio of 1000 implies that the Atwood number for this case is 0.998. The evolution of the bubble, spike, and saddle points for this case are displayed in Fig. 4(b).

Fig. 5 shows the time evolution of the interface between the heavy and light fluids. Here the midplane view of the 3D results show qualitative agreement with available 2D data (Shao and Shu, 2015; Ren et al., 2016; Fakhari et al., 2017b). It is evident that the interfacial traction of the lighter fluid is insufficient to cause the mushroom-like formation of the spike.

Currently, there exist few studies of the Rayleigh–Taylor instability of immiscible fluids with high-density ratios in 2D and or 3D (Ren et al., 2016; Fakhari et al., 2017b). The model presented in this work was not only able to achieve a stable simulation of a high-density ratio flow case, but one with a relatively high Reynolds number as well. This indicates that the solver is sufficiently robust to be applied to practical liquid-gas systems, which is further demonstrated in the following section.

4.3. Taylor bubble investigation

The evolution of Taylor bubbles is observed in a wide range of natural and industrial flows. Understanding the associated physics of these flows can provide critical insight into applications such as the concentration polarisation and fouling of mem-

Please cite this article as: T. Mitchell et al., Development of a three-dimensional phase-field lattice Boltzmann method for the study of immiscible fluids at high density ratios, International Journal of Multiphase Flow (2018), https://doi.org/10.1016/j.ijmultiphaseflow.2018.05.004

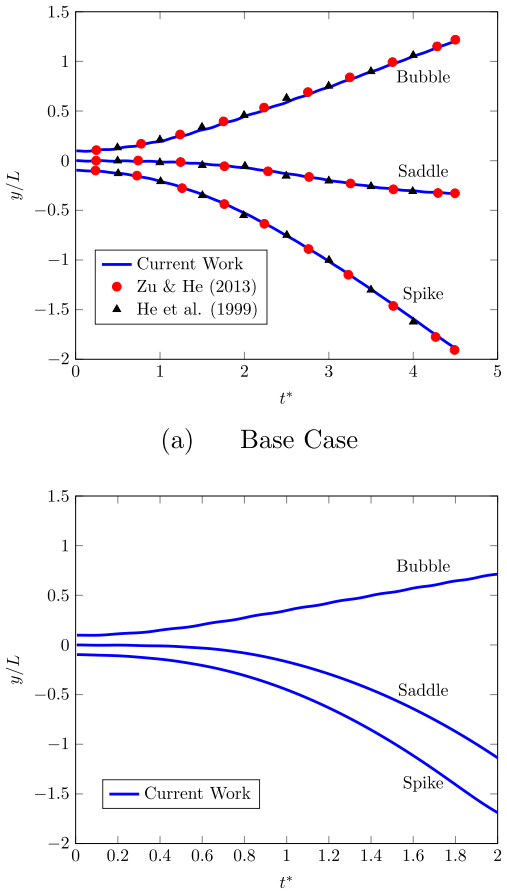

Fig. 4. Time evolution of the bubble front (0, y, 0), the saddle point (0, y, 64) and the spike (64, y, 64) in the case of the Rayleigh–Taylor instability. The base case (a) indicates the evolution with At = 0.500 and Re = 128 while the extension case (b) presents the results with At = 0.998 and Re = 3000.

branes (Ndinisa et al., 2005), and the transportation of hydrocarbons through pipeline systems (Bugg and Saad, 2002; Lizarraga-Garcia et al., 2017). It has been reported in the literature that the rise velocity of a Taylor bubble is a key model parameter used in certain mechanistic modelling frameworks in order to predict liquid hold-up and pressure gradients through piping networks. A full review of the literature investigating the motion of rising Taylor bubbles in vertical pipes is not attempted here, and the interested reader is referred to Lizarraga-Garcia et al. (2017) for an in-depth discussion of the extensive work in this area. The aim of this section is to study the flow features of a Taylor bubble using the numerical simulation techniques presented in Section 3. As such, the macroscopic rise velocity, the local flow field and the interface profile of the bubble will be investigated and compared with experimental work available in the literature (Bugg and Saad, 2002).

The experimental work of Bugg and Saad (2002) has been used by numerous researchers to validate commercial code bases. Lizarraga-Garcia et al. (2017) recently used this data to validate a level-set formulation in the TransAT software developed at ASCOMP. Additionally, the work of Ndinisa et al. (2005) used these experimental results to assess the volume-of-fluid method, two-fluid method, and a combined model available in the CFX 5.6 code from ANSYS. The experimental work was conducted in a vertical tube with diameter $D_T = 19$ mm, filled with olive oil as the working fluid. The relevant dimensionless numbers include the Eötvos number, Eo, which is the ratio of gravitational to interfacial forces, the Morton number, Mo, which assists in defining the expected shape of the bubble, and the Reynolds number, Re_r based on the terminal rise velocity of the bubble, U_t. These are defined as

$$\mathrm{Eo} = \frac{(\rho_\mathrm{H} - \rho_\mathrm{L}) g D_T^2}{\sigma} = 100, \tag{45}$$

$$\mathrm{Mo} = \frac{g \mu_\mathrm{H}^4}{(\rho_\mathrm{H} - \rho_\mathrm{L}) \sigma^3} = 0.015, \tag{46}$$

$$\mathrm{Re}_r = \frac{\rho_\mathrm{H} U_t D_T}{\mu_\mathrm{H}} = 27. \tag{47}$$

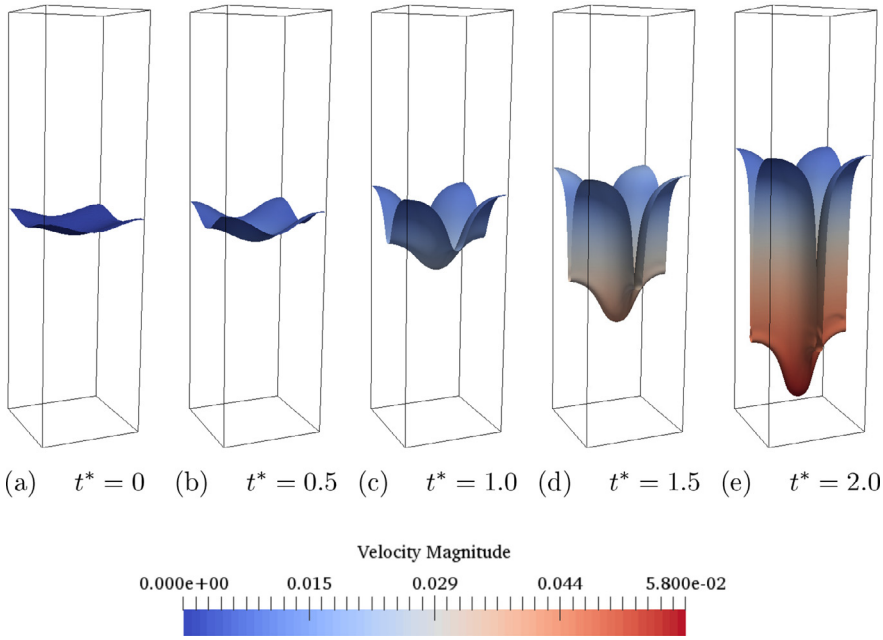

Fig. 5. The evolution of the three-dimensional Rayleigh–Taylor instability with flow conditions defined by At = 0.998, Re = 3000, $\mu^* = 100$, and Ca = 8.7. The model parameters achieve density and viscosity ratios similar to that of an air-water mixture.

Please cite this article as: T. Mitchell et al., Development of a three-dimensional phase-field lattice Boltzmann method for the study of immiscible fluids at high density ratios, International Journal of Multiphase Flow (2018), https://doi.org/10.1016/j.ijmultiphaseflow.2018.05.004

Table 1
Reynolds numbers found with varying numerical techniques including VOF, TFM, and the combined TFM-VOF model from Ndinisa et al. (2005), as well as the current LBM in comparison to the reference experimental (Exp) study (Bugg and Saad, 2002).

Study	Ndinisa et al. (2005)			Bugg and Saad (2002)	$D_T = 64$	$D_T = 128$	$D_T = 256$
Method	VOF	TFM	Combined	Exp	LBM	LBM	LBM
Re	28.9	24.5	22.7	27	27.98	26.99	26.77

For this study, it is assumed that the density and viscosity of the air injected into the olive oil is 1.225 kg/m^3 and 1.983×10^{-5} *Pa.s*, respectively. This gives a density ratio of 744 and a viscosity ratio of 4236, which when combined with the reported olive oil properties (Bugg and Saad, 2002), supplies the five π-groups required to define the bubble dynamics.

Particle image velocimetry (PIV) was used by Bugg and Saad (2002) in order to obtain results for the liquid flow field surrounding the Taylor bubble. Macroscopically, the results of the experiment found a terminal rise velocity of 0.131 m/s which equates to a Froude number of 0.303 ($\mathrm{Fr} = U_t/\sqrt{gD_T}$) and the Reynolds number calculated in Eq. (47). The work done in CFX 5.6 (Ndinisa et al., 2005) was able to provide comparable results to this with terminal velocities of 0.140 m/s, 0.119 m/s, and 0.110 m/s obtained using the volume-of-fluid (VOF) technique, the two-fluid model (TFM), and a combined model, respectively. Here it can be seen that the order of error is within 8%. However, it was reported that the bubble shape was inadequately captured by the VOF technique and the interfacial transition region was excessive for the TFM. The combined model was thus suggested by Ndinisa et al. (2005) to match the flow field measured by Bugg and Saad (2002).

In order to capture the system using the LBM described in this study, one only needs to define a characteristic length (tube diameter) and a time scale in order to derive the remaining simulation parameters from the dimensionless variables stated. Three different resolutions were tested to demonstrate that the results were independent of the grid, with similar findings obtained using 64, 128 and 256 cells across the tube diameter. The time scale for these simulations was defined according to the diffusive scaling such that $t_0 = 2000$, 8000, and 32000 for the different grid resolutions, respectively. A total run time of $10t_0$ was found to be sufficient for convergence of both shape and rise velocity for these cases. The results using $D_T = 128$ are presented here, with the length of the simulation domain specified as $10D_T$. As in the work of Ndinisa et al. (2005), the low density region was initialised as a cylinder with a diameter of $0.75D_T$ and a height of $3D_T$. Fig. 6 shows the time evolution of the bubble, with 3D images showing an iso-plane of $\phi = 0.5$, and a 2D-slice of the phase-field distribution across the pipe diameter. With this simulation the macroscopic bubble rise velocity, the local flow field dynamics about the bubble, and the interface profile in regions of interest can be compared.

4.3.1. Bubble rise velocity

During the simulation, the bubble interface location and interface velocity was recorded to check steady-state convergence. This was approximately achieved at $6 - 7t_0$ depending on the resolution. The rise velocity was then taken as the average of the local velocity between $9t_0$ and $10t_0$. Table 1 provides a comparison of the terminal velocity found in the current study with those from the literature. Here it is seen that the proposed LBM is able to provide a very close match to the experimental data (Bugg and Saad, 2002) for all the resolutions tested, outperforming the previous numerical results (Ndinisa et al., 2005).

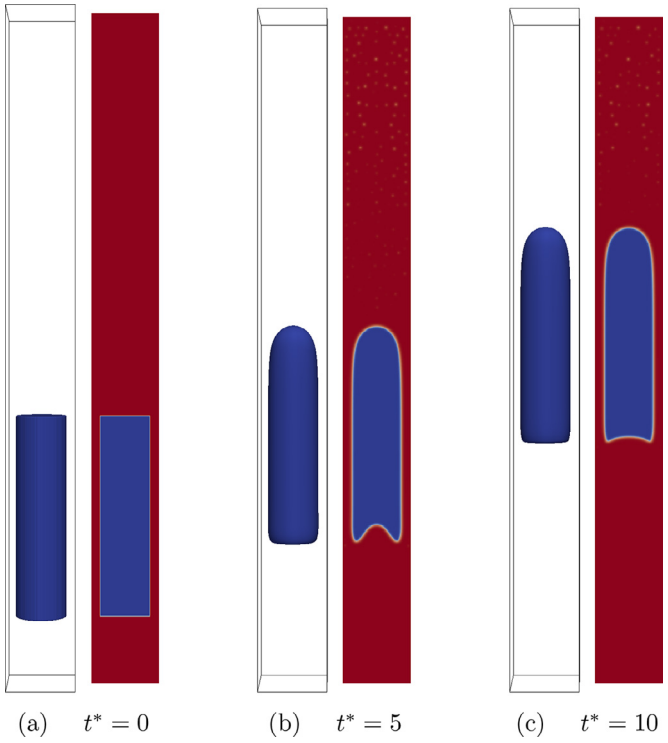

Fig. 6. The evolution of a three-dimensional Taylor bubble inside of a cylindrical tube is shown at time increments of $5t_0$ from left to right. The flow conditions were specified according to the experimental work of Bugg and Saad (2002) with $D_T = 128$, $\rho^* = 744$, $\mathrm{Re}_r \approx 27$, $\mu^* = 4236$, $\mathrm{Mo} = 0.015$, and $\mathrm{Eo} = 100$. In each figure, the right frame indicates the mid-plane view of the simulation domain.

4.3.2. Flow field analysis

The flow field is assessed in the same manner as in previous works by interrogating the velocity field along the tube centreline in front of the bubble nose as well as along four radial lines at various locations relative to the bubble. The locations for the radial lines of interest are given by $0.111D_T$ ahead of the bubble nose, at $0.504D_T$ and $2D_T$ behind the bubble nose where the liquid film is developing and developed, respectively, and at $D_T/5$ behind the bubble in the wake region. It is noted here that the flow behaviour in the wake region changes rapidly, thus with only an approximate location given in the experimental work (Bugg and Saad, 2002), this study provides two additional measurements at $D_T/6$ and $D_T/7$ behind the bubble (measured from the centreline) for comparison. For clarity, these lines have been superimposed onto the interface contour defined at $\phi = 0.5$ in Fig. 7.

Fig. 8 shows that the velocity along the tube axis in front of the bubble nose is captured accurately, with the LBM results matching well with both the experimental and numerical findings in the literature. The figure shows that the bubble has limited influence on the liquid ahead of it, with the velocity decaying to near zero at around $0.3D_T$.

A characteristic of the Taylor bubbles modelled in this regime is the existence of a liquid film between the low density phase and the wall. The development of this film was well reported through

Please cite this article as: T. Mitchell et al., Development of a three-dimensional phase-field lattice Boltzmann method for the study of immiscible fluids at high density ratios, International Journal of Multiphase Flow (2018), https://doi.org/10.1016/j.ijmultiphaseflow.2018.05.004

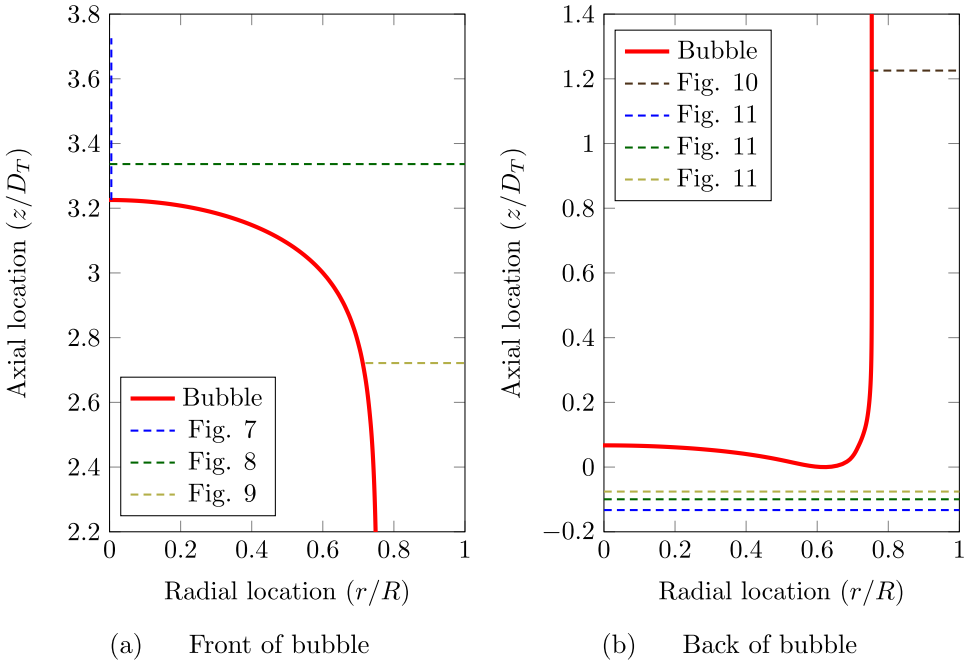

Fig. 7. The location of the flow velocity profiles presented in subsqequent figures are shown relative to the interface position of the (a) front and (b) back of the Taylor bubble.

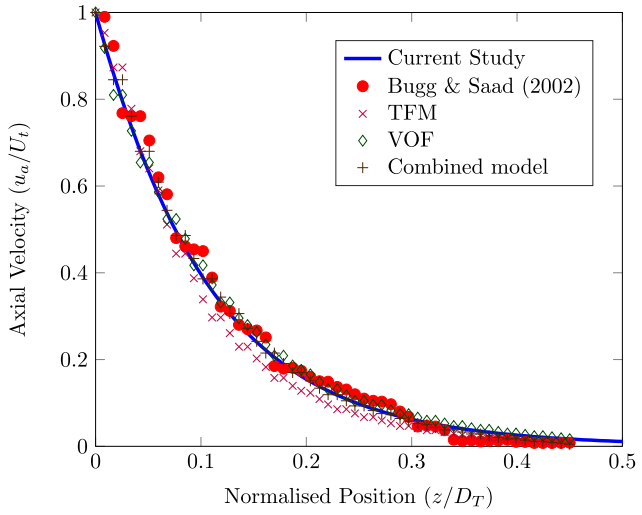

Fig. 8. The profile of the axial velocity, u_a, directly in front of the Taylor bubble. The comparative numerical results including the TFM, VOF, and the combined TFM-VOF model were supplied by Ndinisa et al. (2005).

the PIV experiments providing a further means of validation for the present 3D LBM. Fig. 9 provides a comparison with the axial velocity along a radial line $0.111D_T$ in front of the bubble nose. In agreement with the conclusions of Ndinisa et al. (2005), this figure indicates a transition from upwards to downwards flow of the high density fluid roughly halfway between the tube wall and the central axis. Additionally, the radial profile indicates a strong velocity component above the bubble where the fluid is accelerating into the liquid film region near the tube wall. The model presented in the current work performs in a similar fashion to the numerical methods from the literature, closely matching the axial velocity, but is unable to capture the premature decay in the radial velocity observed at approximately $0.8D_T$ in the experimental results.

The heavy fluid that is forced towards the tube wall by the rising bubble develops into the liquid film. Fig. 10 shows the high axial velocity of the heavy fluid as it propagates downwards surrounding the Taylor bubble. At this point, it is evident that there is still a large radial component of velocity, indicating that the film is still developing. The present LB model is again seen to perform on a similar level of accuracy as the reference numerical methods (Ndinisa et al., 2005).

As the liquid film moves past the elongated bubble, it tends towards a fully-developed profile with negligible velocity in the radial direction and high velocities in the axial direction of the pipe. At this stage, the shear stress at the wall is capable of supporting the weight of the film with zero velocity at the solid contact, but high velocity near the liquid-gas interface where the shear stress is negligible in comparison (Ndinisa et al., 2005). Fig. 11 shows the axial velocity at this stage where it can be observed that the maximum velocity in the liquid film is over twice that of the bubble propagation speed. This result again shows a close agreement between the LBM simulations conducted in this study and the CFX 5.6 results (Ndinisa et al., 2005) as well as the experimental findings (Bugg and Saad, 2002).

When the liquid film moves past the end of the bubble a significant deceleration is observed as flow expands and recirculates in the wake region. Fig. 12 highlights this fact with the axial flow component still downwards in the near wall region, but upwards near the axis of the tube. Additionally, this figure shows that the wake has the region of maximum radial flow as the energy from the liquid film dissipates into the bulk. It is observed that the results from the location $D_T/5$ slightly underpredict the magnitude of axial velocity, but at $D_T/6$ (which is only four computational cells above the $D_T/5$ location) a significantly better match is noted. This could be a result of either the diffuse-interface modelling approach adopted in the LBM algorithm or an uncertainty in the experimental location measurement. Nonetheless, this deviation seems to denote a minor error in comparison to experimental results. To identify possible causes of this discrepancy, an analysis of the bubble shape is undertaken.

Please cite this article as: T. Mitchell et al., Development of a three-dimensional phase-field lattice Boltzmann method for the study of immiscible fluids at high density ratios, International Journal of Multiphase Flow (2018), https://doi.org/10.1016/j.ijmultiphaseflow.2018.05.004

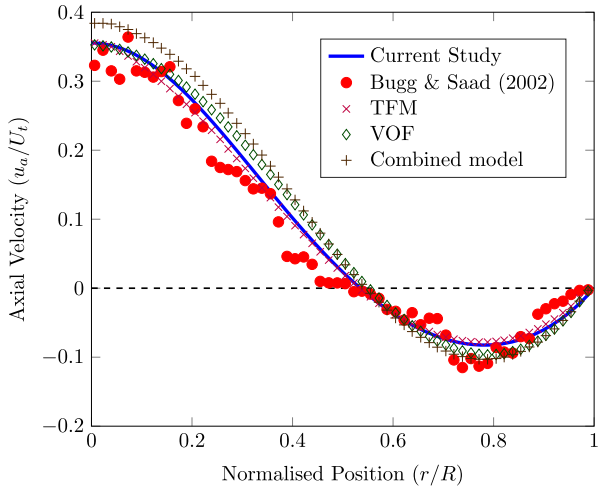

(a) Axial Velocity

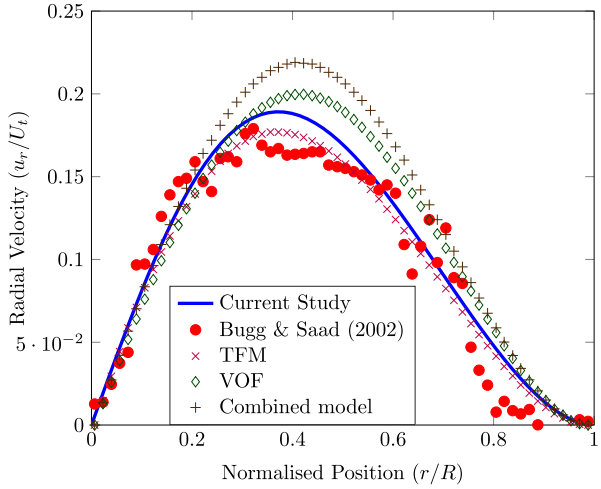

(b) Radial Velocity

Fig. 9. The (a) axial and (b) radial velocity profiles along a radial line positioned $0.111D_T$ above the bubble nose.

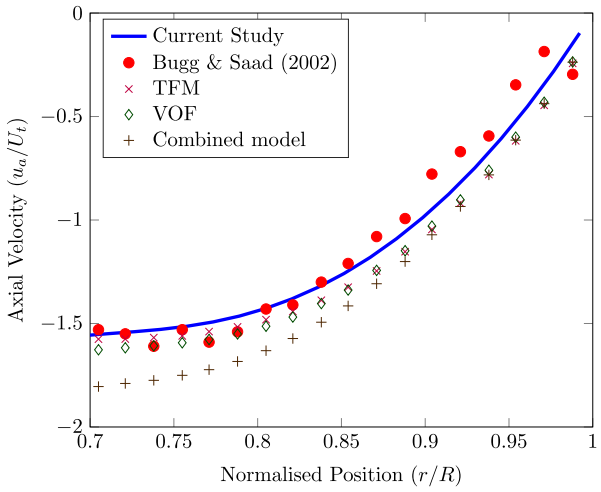

(a) Axial Velocity

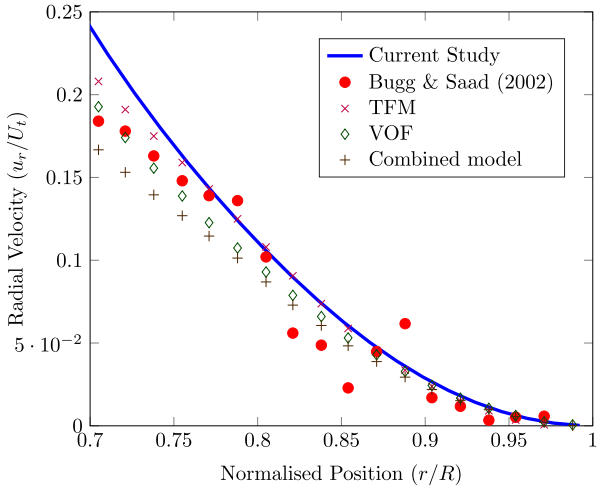

(b) Radial Velocity

Fig. 10. The (a) axial and (b) radial velocity profiles along a radial line positioned $0.504D_T$ behind the bubble nose.

4.3.3. Bubble shape analysis

So far, a detailed comparison of the flow field surrounding the Taylor bubble in relation to experimental (Bugg and Saad, 2002) and numerical (Ndinisa et al., 2005) works available in the literature has been shown. In this section, the key features of the bubble profile in the nose and tail regions are analysed. Furthermore, the profile for various simulation resolutions is presented to demonstrate the grid dependency of the results. The purpose of this is to provide a complete validation and analysis of the macroscopic propagation of Taylor bubbles, the local flow field, and the interface topology.

Fig. 13(a) gives a comparison of the Taylor bubble nose profile using the current LBM and the reference experimental work (Bugg and Saad, 2002). It is noted here that the phase-field model for capturing the interface dynamics is a diffuse interface model, and as such the interface is distributed over a finite distance rather than a singularity. The contour shown here represents the iso-line for which $\phi = 0.5$. A good fit can be seen between the works, however a discrepancy is evident about the radial location of $r/R = 0.5$. The grid dependency of the nose profile is evident with the resolution defined by $D_T = 64$, but is clearly negligible with only minor variation from $D_T = 128$ to $D_T = 256$.

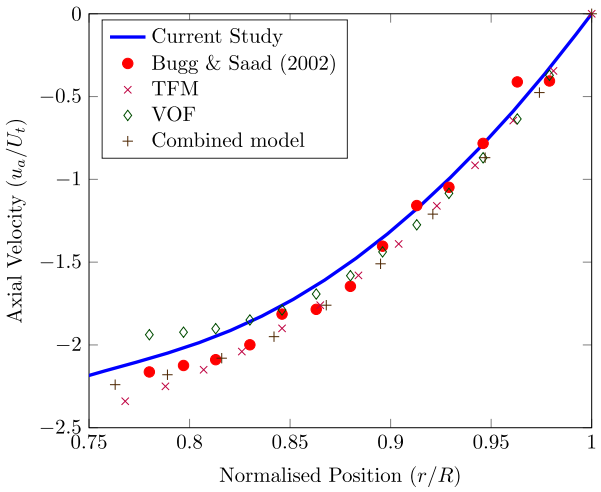

Fig. 11. The axial velocity profile along a radial line positioned $2D_T$ behind the bubble nose.

Please cite this article as: T. Mitchell et al., Development of a three-dimensional phase-field lattice Boltzmann method for the study of immiscible fluids at high density ratios, International Journal of Multiphase Flow (2018), https://doi.org/10.1016/j.ijmultiphaseflow.2018.05.004

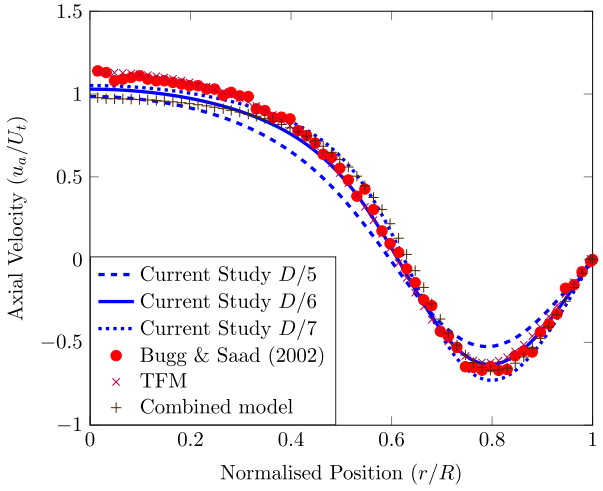

(a) Axial Velocity

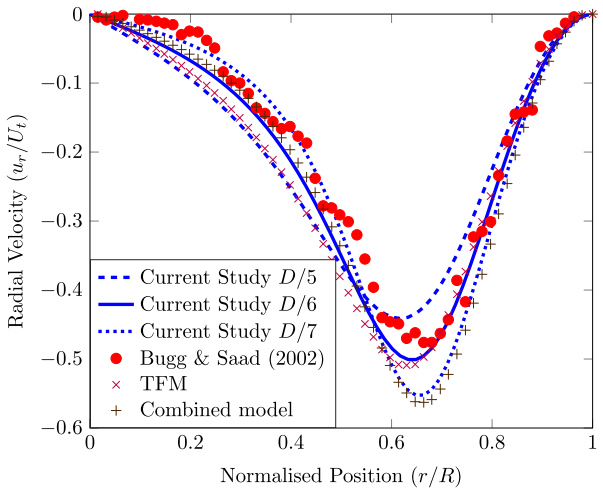

(b) Radial Velocity

Fig. 12. The (a) axial and (b) radial velocity profiles along radial lines positioned behind the bubble (in the wake region) at distances of $D_T/5$, $D_T/6$, and $D_T/7$.

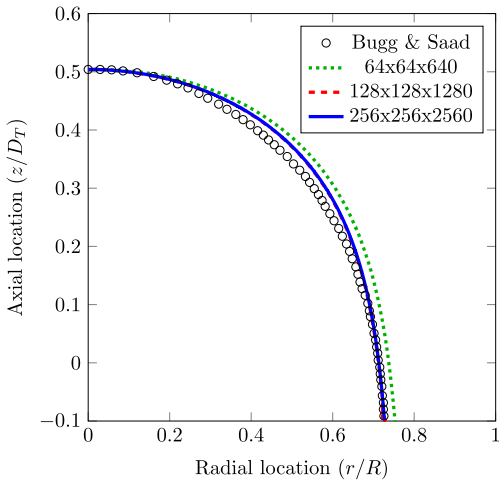

(a) Bubble front profile

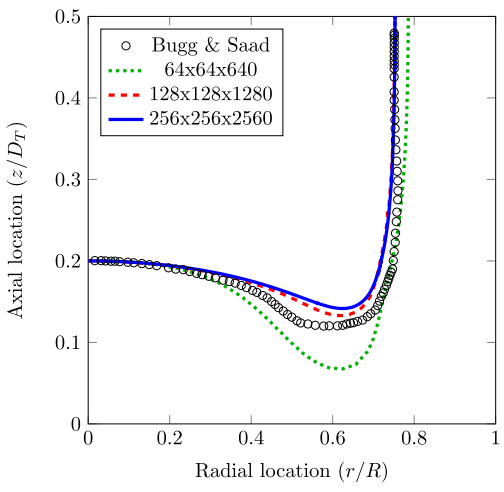

(b) Bubble tail profile

Fig. 13. The profiles of the Taylor bubble interface are indicated by the contour of $\phi = 0.5$ in the LBM results. Here the vertical location is given with reference to an arbitrary location: (a) the front of the bubble is defined at a dimensionless height of 0.5; (b) the centreline of the interface tail is defined at a dimensionless height of 0.2. The interface profile is compared with the reference PIV experiments (Bugg and Saad, 2002).

Fig. 13(b) indicates the profile about the tail of the Taylor bubble for various resolutions. Here the discrepancy between experiment and numerics is more pronounced. Additionally, the grid resolution is observed to have a higher influence on the interface topology, particularly for the lowest resolution of $D_T = 64$. The converged shape of the higher resolution tests seemingly do not capture the lower bubble tail observed in experimental measurements, with an error of approximately 20% observed at $r/R \approx 0.52$. The discrepancy in the shape is likely the cause of the minor deviations observed in the flow field of the wake presented in Fig. 12. In particular, the elongation observed in the tail of the experimental bubble could be expected to lead to a greater axial, but lower radial velocity component near the tube centerline. This occurs as a result of the expansion of the liquid film at a location closer to the measurement point ($D/5$ below the central axis of the bubble). This is further verified by the numerical results presented at a location of $D/6$, which provide a close fit to experimental data. Qualitatively, the reduced elongation observed numerically agrees with the findings presented in Fig. 10 of Ndinisa et al. (2005).

In this section, it has been shown that the phase-field LBM is able to accurately capture the Taylor bubble rise velocity, the local flow field about the bubble, and the interface profile in key areas of interest around the bubble. The calculated rise velocity appeared to match better to experimental results than the previous numerical work, while the local flow field showed only minor discrepancies. The convergence of the interface profile was observed at a computational resolution of $D_T = 128$, with the shapes matching closely with experimental PIV results. The accuracy of results further highlights the capability of the present 3D model to capture practical flows of interest.

5. Summary and conclusion

This work presented the development of a phase-field LBM in three dimensions. The model was benchmarked and validated against numerical and experimental works. The use of a weighted multiple-relaxation-time collision scheme enhanced the numerical stability of the model, enabling the simulation of high density ratios and high Reynolds numbers. The model itself employs the conservative phase-field LBE designed to simulate immiscible fluids coupled with a velocity-based LBE to recover the system hydrody-

Please cite this article as: T. Mitchell et al., Development of a three-dimensional phase-field lattice Boltzmann method for the study of immiscible fluids at high density ratios, International Journal of Multiphase Flow (2018), https://doi.org/10.1016/j.ijmultiphaseflow.2018.05.004

namics at high density ratios. The current model contains just one non-local parameter in the LB collision step, offering an improved locality in comparison with other available LB models.

The performance of the model for density-matched drop deformation, a common case used in the benchmarking of certain LB models, was first demonstrated. Here, similar performance to published results using a colour-gradient model was observed, with theoretical results being reasonably well matched in the low capillary number limit. Similarly to the existing LB models, the present LBM upheld useful features such as an easily adjustable surface tension and a maintained interface thickness.

Flow cases where the density contrast of the fluids have a significant impact on the system dynamics were also investigated. This included the Rayleigh–Taylor instability in 3D. A slight interface perturbation was introduced causing the heavy fluid to characteristically penetrate into the lighter one. The model was benchmarked against the previous case in which a density ratio of three was used and a mushroom-like roll-up of the heavy fluid spike was observed. From here, the model was extended beyond previously discussed literature by simulating the Rayleigh–Taylor instability with fluids similar in properties to an air-water system. The system was observed to capture the dynamics of such a system stably up to relatively high Reynolds numbers.

Having verified the model with the previous numerical tests, validation against experimental results investigating the rise of a Taylor bubble in a quiescent fluid was sought. The experiment injected an air bubble into a tube filled with olive oil and utilised PIV technology to capture high resolution flow field data. The phase-field LBM was not only able to recover the observed rise velocity reported in experiments, but the local flow field data about the bubble was also accurately matched. The steady-state interface profile about the bubble nose and tail was extracted from simulations and compared with that found experimentally. Minor discrepancies were observed, but overall the results were deemed to capture the physical system, providing a detailed validation case for the model presented.

Further validation and application of the model within industrially relevant problems will be an area of ongoing research. Of particular interest is the piped transport of multiphase fluids present in the oil and gas, chemical, and nuclear industries. In these cases, factors such as flow direction, angle of inclination, and piping configurations (*e.g.* annular designs) can complicate the flow dynamics and phase interactions.

Acknowledgements

TM would like to acknowledge the support of the Australian Government Research Training Program Scholarship during the development of this work. This work was supported by resources provided by the Pawsey Supercomputing Centre with funding from the Australian Government and the Government of Western Australia. Thanks also goes to the authors of the *open-source* lattice Boltzmann framework, TCLB (https://github.com/CFD-GO/TCLB), Łukasz Łaniewski-Wołłk and Michał Dzikowski. Jon McCullough is also acknowledged for insightful discussions and proofing comments on the manuscript.

Appendix A. Lattice velocity sets and weightings

The discrete velocity set for the D3Q15 lattice used for the conservative phase-field equation is given by,

$$\boldsymbol{c}_{15} = \begin{pmatrix} c_x \\ c_y \\ c_z \end{pmatrix} = \begin{pmatrix} 0 & 1 & -1 & 0 & 0 & 0 & 0 & 1 & -1 & 1 & -1 & 1 & -1 & 1 & -1 \\ 0 & 0 & 0 & 1 & -1 & 0 & 0 & 1 & 1 & -1 & -1 & 1 & 1 & -1 & -1 \\ 0 & 0 & 0 & 0 & 0 & 1 & -1 & 1 & 1 & 1 & 1 & -1 & -1 & -1 & -1 \end{pmatrix}. \tag{A.1}$$

The corresponding lattice weights are given by,

$$w_i = \frac{1}{72} \begin{cases} 16, & i = 0, \\ 8, & i = 1-6, \\ 1, & i = 7-14. \end{cases} \tag{A.2}$$

As for the discrete velocity set of the D3Q27 lattice used for the hydrodynamics, a slightly unconventional ordering was used in order to align the first 15 velocity directions with the D3Q15 model,

$$\boldsymbol{c}_{27} = \begin{pmatrix} c_x \\ c_y \\ c_z \end{pmatrix} \tag{A.3}$$

$$= \begin{pmatrix} c_{0-14,x} & 1 & -1 & 1 & -1 & 1 & -1 & 1 & -1 & 0 & 0 & 0 & 0 \\ c_{0-14,y} & 1 & 1 & -1 & -1 & 0 & 0 & 0 & 0 & 1 & -1 & 1 & -1 \\ c_{0-14,z} & 0 & 0 & 0 & 0 & 1 & 1 & -1 & -1 & 1 & 1 & -1 & -1 \end{pmatrix}. \tag{A.4}$$

The corresponding lattice weights are then given by,

$$w_i = \frac{1}{216} \begin{cases} 64, & i = 0, \\ 16, & i = 1-6, \\ 1, & i = 7-14, \\ 4, & i = 15-26. \end{cases} \tag{A.5}$$

Appendix B. WMRT construction for the D3Q27 lattice

For a full definition of the WMRT the interested reader is pointed to the work of Fakhari et al. (2017a). Here, only the information required for implementation is given. It is worth mentioning that a correction was noted for the fourth-order moment $\mathbf{m}_{17}$ as well as the fifth- and sixth-order moments, although the final transformation matrix given in Fakhari et al. (2017a) was accurate. The correct weighted moments making up the transformation matrix are given by:

Zeroth-order:

$$\mathbf{m}_0 = 1$$

First-order:

$$\mathbf{m}_1 = c_{i,x}$$
$$\mathbf{m}_2 = c_{i,y}$$
$$\mathbf{m}_3 = c_{i,z}$$

Second-order:

$$\mathbf{m}_4 = c_{i,x}c_{i,y}$$
$$\mathbf{m}_5 = c_{i,y}c_{i,z}$$
$$\mathbf{m}_6 = c_{i,z}c_{i,x}$$
$$\mathbf{m}_7 = 3c_{i,x}^2 - |\boldsymbol{c}_i|^2$$
$$\mathbf{m}_8 = c_{i,y}^2 - c_{i,z}^2$$
$$\mathbf{m}_9 = |\boldsymbol{c}_i|^2 - 1$$

Third-order:

$$\mathbf{m}_{10} = c_{i,x}(3|\boldsymbol{c}_i|^2 - 5)$$
$$\mathbf{m}_{11} = c_{i,y}(3|\boldsymbol{c}_i|^2 - 5)$$
$$\mathbf{m}_{12} = c_{i,z}(3|\boldsymbol{c}_i|^2 - 5)$$
$$\mathbf{m}_{13} = c_{i,x}(c_{i,y}^2 - c_{i,z}^2)$$

Please cite this article as: T. Mitchell et al., Development of a three-dimensional phase-field lattice Boltzmann method for the study of immiscible fluids at high density ratios, International Journal of Multiphase Flow (2018), https://doi.org/10.1016/j.ijmultiphaseflow.2018.05.004

$\mathbf{m}_{14} = c_{i,y}(c_{i,z}^2 - c_{i,x}^2)$

$\mathbf{m}_{15} = c_{i,z}(c_{i,x}^2 - c_{i,y}^2)$

$\mathbf{m}_{16} = c_{i,x}c_{i,y}c_{i,z}$

Fourth-order:

$\mathbf{m}_{17} = 0.5(3|\boldsymbol{c}_i|^4 - 7|\boldsymbol{c}_i|^2 + 2)$

$\mathbf{m}_{18} = (3|\boldsymbol{c}_i|^2 - 4)(3c_{i,x}^2 - |\boldsymbol{c}_i|^2)$

$\mathbf{m}_{19} = (3|\boldsymbol{c}_i|^2 - 4)(c_{i,y}^2 - c_{i,z}^2)$

$\mathbf{m}_{20} = c_{i,x}c_{i,y}(3|\boldsymbol{c}_i|^2 - 7)$

$\mathbf{m}_{21} = c_{i,y}c_{i,z}(3|\boldsymbol{c}_i|^2 - 7)$

$\mathbf{m}_{22} = c_{i,z}c_{i,x}(3|\boldsymbol{c}_i|^2 - 7)$

Fifth-order:

$\mathbf{m}_{23} = 0.5c_{i,x}(9|\boldsymbol{c}_i|^4 - 33|\boldsymbol{c}_i|^2 + 26)$

$\mathbf{m}_{24} = 0.5c_{i,y}(9|\boldsymbol{c}_i|^4 - 33|\boldsymbol{c}_i|^2 + 26)$

$\mathbf{m}_{25} = 0.5c_{i,z}(9|\boldsymbol{c}_i|^4 - 33|\boldsymbol{c}_i|^2 + 26)$

Sixth-order:

$\mathbf{m}_{26} = 0.5(9|\boldsymbol{c}_i|^6 - 36|\boldsymbol{c}_i|^4 + 33|\boldsymbol{c}_i|^2 - 2)$

With these moments and the defined velocity vector, the weighted transformation matrix for the D3Q27 lattice becomes:

$$\mathbf{M} = \begin{pmatrix}
1 & 1 & 1 & 1 & 1 & 1 & 1 & 1 & 1 & 1 & 1 & 1 & 1 & 1 & 1 & 1 & 1 & 1 & 1 & 1 & 1 & 1 & 1 & 1 & 1 & 1 & 1 \\
0 & 1 & -1 & 0 & 0 & 0 & 0 & 1 & -1 & 1 & -1 & 1 & -1 & 1 & -1 & 1 & -1 & 1 & -1 & 1 & -1 & 1 & -1 & 0 & 0 & 0 & 0 \\
0 & 0 & 0 & 1 & -1 & 0 & 0 & 1 & 1 & -1 & -1 & 1 & 1 & -1 & -1 & 1 & 1 & -1 & -1 & 0 & 0 & 0 & 0 & 1 & -1 & 1 & -1 \\
0 & 0 & 0 & 0 & 0 & 1 & -1 & 1 & 1 & 1 & 1 & -1 & -1 & -1 & -1 & 0 & 0 & 0 & 0 & 1 & 1 & -1 & -1 & 1 & 1 & -1 & -1 \\
0 & 0 & 0 & 0 & 0 & 0 & 0 & 1 & -1 & -1 & 1 & 1 & -1 & -1 & 1 & 1 & -1 & -1 & 1 & 0 & 0 & 0 & 0 & 0 & 0 & 0 & 0 \\
0 & 0 & 0 & 0 & 0 & 0 & 0 & 1 & 1 & -1 & -1 & -1 & -1 & 1 & 1 & 0 & 0 & 0 & 0 & 0 & 0 & 0 & 0 & 1 & -1 & -1 & 1 \\
0 & 0 & 0 & 0 & 0 & 0 & 0 & 1 & -1 & 1 & -1 & -1 & 1 & -1 & 1 & 0 & 0 & 0 & 0 & 1 & -1 & -1 & 1 & 0 & 0 & 0 & 0 \\
0 & 2 & 2 & -1 & -1 & -1 & -1 & 0 & 0 & 0 & 0 & 0 & 0 & 0 & 0 & 1 & 1 & 1 & 1 & 1 & 1 & 1 & 1 & -2 & -2 & -2 & -2 \\
0 & 0 & 0 & 1 & 1 & -1 & -1 & 0 & 0 & 0 & 0 & 0 & 0 & 0 & 0 & 1 & 1 & 1 & 1 & -1 & -1 & -1 & -1 & 0 & 0 & 0 & 0 \\
-1 & 0 & 0 & 0 & 0 & 0 & 0 & 2 & 2 & 2 & 2 & 2 & 2 & 2 & 2 & 1 & 1 & 1 & 1 & 1 & 1 & 1 & 1 & 1 & 1 & 1 & 1 \\
0 & -2 & 2 & 0 & 0 & 0 & 0 & 4 & -4 & 4 & -4 & 4 & -4 & 4 & -4 & 1 & -1 & 1 & -1 & 1 & -1 & 1 & -1 & 0 & 0 & 0 & 0 \\
0 & 0 & 0 & -2 & 2 & 0 & 0 & 4 & 4 & -4 & -4 & 4 & 4 & -4 & -4 & 1 & 1 & -1 & -1 & 0 & 0 & 0 & 0 & 1 & -1 & 1 & -1 \\
0 & 0 & 0 & 0 & 0 & -2 & 2 & 4 & 4 & 4 & 4 & -4 & -4 & -4 & -4 & 0 & 0 & 0 & 0 & 1 & 1 & -1 & -1 & 1 & 1 & -1 & -1 \\
0 & 0 & 0 & 0 & 0 & 0 & 0 & 0 & 0 & 0 & 0 & 0 & 0 & 0 & 0 & 1 & -1 & 1 & -1 & -1 & 1 & -1 & 1 & 0 & 0 & 0 & 0 \\
0 & 0 & 0 & 0 & 0 & 0 & 0 & 0 & 0 & 0 & 0 & 0 & 0 & 0 & 0 & -1 & -1 & 1 & 1 & 0 & 0 & 0 & 0 & 1 & -1 & 1 & -1 \\
0 & 0 & 0 & 0 & 0 & 0 & 0 & 0 & 0 & 0 & 0 & 0 & 0 & 0 & 0 & 0 & 0 & 0 & 0 & 1 & 1 & -1 & -1 & -1 & -1 & 1 & 1 \\
0 & 0 & 0 & 0 & 0 & 0 & 0 & 1 & -1 & -1 & 1 & -1 & 1 & 1 & -1 & 0 & 0 & 0 & 0 & 0 & 0 & 0 & 0 & 0 & 0 & 0 & 0 \\
1 & -1 & -1 & -1 & -1 & -1 & -1 & 4 & 4 & 4 & 4 & 4 & 4 & 4 & 4 & 0 & 0 & 0 & 0 & 0 & 0 & 0 & 0 & 0 & 0 & 0 & 0 \\
0 & -2 & -2 & 1 & 1 & 1 & 1 & 0 & 0 & 0 & 0 & 0 & 0 & 0 & 0 & 2 & 2 & 2 & 2 & 2 & 2 & 2 & 2 & -4 & -4 & -4 & -4 \\
0 & 0 & 0 & -1 & -1 & 1 & 1 & 0 & 0 & 0 & 0 & 0 & 0 & 0 & 0 & 2 & 2 & 2 & 2 & -2 & -2 & -2 & -2 & 0 & 0 & 0 & 0 \\
0 & 0 & 0 & 0 & 0 & 0 & 0 & 2 & -2 & -2 & 2 & 2 & -2 & -2 & 2 & -1 & 1 & 1 & -1 & 0 & 0 & 0 & 0 & 0 & 0 & 0 & 0 \\
0 & 0 & 0 & 0 & 0 & 0 & 0 & 2 & 2 & -2 & -2 & -2 & -2 & 2 & 2 & 0 & 0 & 0 & 0 & 0 & 0 & 0 & 0 & -1 & 1 & 1 & -1 \\
0 & 0 & 0 & 0 & 0 & 0 & 0 & 2 & -2 & 2 & -2 & -2 & 2 & -2 & 2 & 0 & 0 & 0 & 0 & -1 & 1 & 1 & -1 & 0 & 0 & 0 & 0 \\
0 & 1 & -1 & 0 & 0 & 0 & 0 & 4 & -4 & 4 & -4 & 4 & -4 & 4 & -4 & -2 & 2 & -2 & 2 & -2 & 2 & -2 & 2 & 0 & 0 & 0 & 0 \\
0 & 0 & 0 & 1 & -1 & 0 & 0 & 4 & 4 & -4 & -4 & 4 & 4 & -4 & -4 & -2 & -2 & 2 & 2 & 0 & 0 & 0 & 0 & -2 & 2 & -2 & 2 \\
0 & 0 & 0 & 0 & 0 & 1 & -1 & 4 & 4 & 4 & 4 & -4 & -4 & -4 & -4 & 0 & 0 & 0 & 0 & -2 & -2 & 2 & 2 & -2 & -2 & 2 & 2 \\
-1 & 2 & 2 & 2 & 2 & 2 & 2 & -8 & 8 & 8 & 8 & 8 & 8 & 8 & 8 & -4 & -4 & -4 & -4 & -4 & -4 & -4 & -4 & -4 & -4 & -4 & -4
\end{pmatrix}$$

Please cite this article as: T. Mitchell et al., Development of a three-dimensional phase-field lattice Boltzmann method for the study of immiscible fluids at high density ratios, International Journal of Multiphase Flow (2018), https://doi.org/10.1016/j.ijmultiphaseflow.2018.05.004

References

Amaya-Bower, L., Lee, T., 2010. Single bubble rising dynamics for moderate Reynolds number using lattice Boltzmann method. Comput. Fluids 39, 1191–1207.
Ammar, S., Pernaudat, G., Trépanier, J., 2017. A multiphase three-dimensional multi-relaxation time (MRT) lattice Boltzmann model with surface tension adjustment. J. Comput. Phys. 343, 73–91.
Ansumali, S., Karlin, I., Ottinger, H., 2003. Minimal entropic kinetic models for hydrodynamics. Europhys. Lett. 63 (6), 798.
Anwar, S., 2013. Lattice Boltzmann modelling of buoyant rise of single and multiple bubbles. Comput. Fluids 88, 430–439.
Atif, M., Kolluru, P., Thantanapally, C., Ansumali, S., 2017. Essentially Entropic Lattice Boltzmann Model. Phys. Rev. Lett. 119, 240602.
Bugg, J.D., Saad, G.A., 2002. The velocity field around a Taylor bubble rising in a stagnant viscous fluid: numerical and experimental results. Int. J. Multiph. Flow 28, 791–803.
Chiu, P.-H., Lin, Y.-T., 2011. A conservative phase field method for solving incompressible two-phase flows. J. Comput. Phys. 230, 185–204.
Danielson, T., 2012. Transient multiphase flow: Past, present and future with flow assurance perspective. Energy Fuels 26, 4137–4144.
Fakhari, A., Bolster, D., Luo, L.-S., 2017a. A weighted multiple-relaxation-time lattice Boltzmann method for multiphase flows and its application to partial coalescence cascades. J. Comput. Phys. 341, 22–43.
Fakhari, A., Geier, M., Bolster, D., 2016a. A simple phase-field model for interface tracking in three dimensions. Comput. Math. Appl..
Fakhari, A., Geier, M., Lee, T., 2016b. A mass-conserving lattice Boltzmann method with dynamic grid refinement for immiscible two-phase flows. J. Comput. Phys. 315, 434–457.
Fakhari, A., Lee, T., 2013. Multiple-relaxation-time lattice Boltzmann method for immiscible fluids at high Reynolds numbers. Phys. Rev. E 87, 023304.
Fakhari, A., Mitchell, T., Leonardi, C., Bolster, D., 2017b. Improved locality of the phase-field lattice Boltzmann model for immiscible fluids at high density ratios. Phys. Rev. E 96 (5), 053301.
Fakhari, A., Rahimian, M.H., 2010. Phase-field modeling by the method of lattice Boltzmann equations. Phys. Rev. E 81, 036707.
Geier, M., Fakhari, A., Lee, T., 2015. Conservative phase-field lattice Boltzmann model for interface tracking equation. Phys. Rev. E 91, 063309.
Geier, M., Schönherr, M., Pasquali, A., Krafczyk, M., 2015. The cumulant lattice Boltzmann equation in three dimensions: theory and validation. Comp. Math. Appl. 70, 507–547.
Grunau, D., Chen, S., Eggert, K., 1993. A lattice bOltzmann model for multiphase fluid flows. Phys. Fluids A 5, 2557.
Gunstensen, A.K., Rothman, D.H., Zaleski, S., Zanetti, G., 1991. Lattice bOltzmann model of immiscible fluids. Phys. Rev. A 43, 4320.
He, X., Chen, S., Zhang, R., 1999. A lattice bOltzmann scheme for incompressible multiphase flow and its application in simulation of rayleigh-Taylor instability. J. Comput. Phys. 152, 642.
Hecht, M., Harting, J., 2010. Implementation of on-site velocity boundary conditions for D3Q19 lattice Boltzmann. J. Stat. Mech. 2010, P01018.
Hirt, C., Nichols, B., 1981. Volume of fluid (VOF) method for the dynamics of free boundaries. J. Comput. Phys. 39, 201–225.
Inamuro, T., Ogata, T., Tajima, S., Konishi, N., 2004. A lattice Boltzmann method for incompressible two-phase flows with large density differences. J. Comput. Phys. 198, 628.
Inamuro, T., Tomita, R., Ogino, F., 2002. Lattice Boltzmann simulations of drop deformation and breakup in shear flows. Int. J. Mod. Phys. B 17 (1 & 2), 21–26.
Jacqmin, D., 1999. Calculation of two-phase Navier–Stokes flows using phase-field modeling. J. Comput. Phys. 155, 96.
Jacqmin, D., 2000. Contact-line dynamics of a diffuse fluid interface. J. Fluid Mech. 402, 57–88.
Komrakova, A., Shardt, O., Eskin, D., Derksen, J., 2014. Lattice Boltzmann simulations of drop deformation and breakup in shear flow. Int. J. Multiph. Flow 59, 24–43.
Kumar, A., 2004. Isotropic finite-differences. J. Comput. Phys. 201, 109–118.
Kupershtokh, A., Medvedev, D., Karpov, D., 2009. On equations of state in a lattice Boltzmann method. Comput. Math. Appl. 58 (5), 965–974.
Łaniewski-Wołłk, L., Rokicki, J., 2016. Adjoint Lattice Boltzmann for topology optimization on multi-GPU architecture. Comput. Math. Appl. 71 (3), 833–848.
Latva-Kokko, M., Rothman, D., 2005. Diffusion properties of gradient-based lattice Boltzmann models of immiscible fluids. Phys. Rev. E 71, 056702.
Leclaire, S., Parmigiani, A., Chopard, B., Latt, J., 2017. Three-dimensional lattice Boltzmann method benchmarks between color-gradient and pseudo-potential immiscible multi-component models. Int. J. Modern Phys. C 28 (7), 1750085.
Leclaire, S., Reggio, M., Trépanier, J., 2012. Numerical evaluation of two recoloring operator for an immiscible two-phase flow lattice Boltzmann model. Appl. Math. Model. 36, 2237–2252.
Lee, T., Lin, C.-L., 2005. A stable discretization of the lattice Boltzmann equation for simulation of incompressible two-phase flows at high density ratio. J. Comput. Phys. 206, 16.
Lee, T., Lin, C.-L., Chen, L.-D., 2006. A lattice Boltzmann algorithm for calculation of the laminar jet diffusion flame. J. Comput. Phys. 215, 133–152.
Lee, T., Liu, L., 2010. Lattice Boltzmann simulations of micron-scale drop impact on dry surfaces. J. Comput. Phys. 229, 8045.
Li, Q., Luo, K.H., Gao, Y.J., He, Y.L., 2012. Additional interfacial force in lattice Boltzmann models for incompressible multiphase flows. Phys. Rev. E 85, 026704.
Liu, H., Kang, Q., Leonardi, C.R., Schmieschek, S., Narváez, A., Jones, B.D., Williams, J.R., Valocchi, A.J., Harting, J., 2016. Multiphase lattice Boltzmann simulations for porous media applications. Comput. Geosci. 20, 777–805.
Liu, H., Valocchi, A.J., Kang, Q., 2012. Three-dimensional lattice Boltzmann model for immiscible two-phase flow simulations. Phys. Rev. E 85, 046309.
Lizarraga-Garcia, E., Buongiorno, J., Al-Safran, E., Lakehal, D., 2017. A broadly-applicable unified closure relation for Taylor bubble rise velocity in pipes with stagnant liquid. Int. J. Multiph. Flow 89, 345–358.
Lycett-Brown, D., Lou, K.H., Liu, R., Lv, P., 2014. Binary droplet collision simulations by a multiphase ccascade lattice Boltzmann method. Phys. Fluids 26, 023303.
Lycett-Brown, D., Luo, K., 2016. Cascaded lattice Boltzmann method with improved forcing scheme for large-density-ratio multiphase flow at high Reynolds and Weber numbers. Phys. Rev. E 94, 053313.
Mazloomi, A., Chikatamarla, S., Karlin, I., 2015. Entropic lattice Boltzmann method for multiphase flows. Phys. Rev. Lett. 114, 174502.
Montessori, A., Falcucci, G., Rocca, M.L., Ansumali, S., Succi, S., 2015. Three-dimensional lattice pseudo-potentials for multiphase flow simulations at high density ratios. J. Stat. Phys. 161, 1404–1419.
Ndinisa, N.V., Wiley, D.E., Fletcher, D.F., 2005. Computational fluid dynamics simulations of Taylor bubbles in tubular membranes: model validation and application to laminar flow systems. Chem. Eng. Res. Des. 83 (A1), 40–49.
Osher, S., Sethian, J.A., 1988. Fronts propagating with curvature dependent speed: Algorithms based on Hamilton–Jacobi formulations. J. Comput. Phys. 79, 12–49.
Porter, M., Coon, E., Kang, Q., Moulton, J., Carey, J., 2012. Multicomponent interparticle-potential lattice Boltzmann model for fluids with large viscosity ratios. Phys. Rev. E 86, 036701.
Ramadugu, R., Thampi, S., Adhikari, R., Succi, S., Ansumali, S., 2013. Lattice differential operators for computational physics. Europhys. Lett. 101, 50006.
Ren, F., Song, B., Sukop, M.C., Hu, H., 2016. Improved lattice Boltzmann modeling of binary flow based on the conservative Allen–Cahn equation. Phys. Rev. E 94, 023311.
Ries, T., Phillips, T., 2007. Lattice Boltzmann model for simulating immiscible two-phase flows. J. Phys. A Math. Theor. 40, 4033.
Shan, X., Chen, H., 1993. Lattice Boltzmann model for simulating flows with multiple phases and components. Phys. Rev. E 47, 1815.
Shan, X., Chen, H., 1994. Simulation of nonideal gases and liquid-gas phase transitions by the lattice Boltzmann equation. Phys. Rev. E 49, 2941.
Shan, X., Doolen, G.D., 1995. Multicomponent lattice-Boltzmann model with interparticle interaction. J. Stat. Phys. 81, 379.
Shao, J., Shu, C., 2015. A hybrid phase field multiple relaxation time lattice Boltzmann method for the incompressible multiphase flow with large density contrast. Int. J. Numer. Meth. Fluids 77, 526–543.
Shapira, M., Haber, S., 1990. Low Reynolds number motion of a droplet in shear flow including wall effects. Int. J. Multiph. Flow 16 (2), 305–321.
van der Sman, R., van der Graaf, S., 2008. Emulsion droplet deformation and breakup with lattice Boltzmann model. Comput. Phys. Commun. 178, 492–504.
Sun, Y., Beckermann, C., 2007. Sharp interface tracking using the phase-field equation. J. Comput. Phys. 220, 626–653.
Swift, M.R., Orlandini, E., Osborn, W.R., Yeomans, J.M., 1996. Lattice bOltzmann simulations of liquid-gas and binary fluid systems. Phys. Rev. E 54, 5041.
Swift, M.R., Osborn, W.R., Yeomans, J.M., 1995. Lattice Boltzmann simulation of nonideal fluids. Phys. Rev. Lett. 75, 830.
Taylor, G.I., 1934. The formation of emulsions in definable fields of flow. P. Roy. Soc. A Math. Phy. 146, 501–523.
Thampi, S., Ansumali, S., Adhikari, R., Succi, S., 2013. Isotropic discrete Laplacian operators from lattice hydrodynamics. J. Comput. Phys. 234, 1–7.
Wu, B., Firouzi, M., Mitchell, T., Rufford, T., Leonardi, C., Towler, B., 2017. A critical review of flow maps for gas-liquid flows in vertical pipes and annuli. Chem. Eng. J. 326, 350–377.
Xi, H., Duncan, C., 1999. Lattice Boltzmann simulations of three-dimensional single droplet deformation and breakup under simple shear flow. Phys. Rev. E 59 (3), 3022.
Yuan, P., Schaefer, L., 2006. Equations of state in a lattice Boltzmann model. Physics of Fluids 18, 042101.
Zheng, H.W., Shu, C., Chew, Y.T., 2006. A lattice Boltzmann model for multiphase flows with large density ratio. J. Comput. Phys. 218, 353.
Zu, Y.Q., He, S., 2013. Phase-field-based lattice Boltzmann model for incompressible binary fluid systems with density and viscosity contrasts. Phys. Rev. E 87, 043301.

Please cite this article as: T. Mitchell et al., Development of a three-dimensional phase-field lattice Boltzmann method for the study of immiscible fluids at high density ratios, International Journal of Multiphase Flow (2018), https://doi.org/10.1016/j.ijmultiphaseflow.2018.05.004